

© 2011 Brian Jon Dellabetta

Report Documentation Page			Form Approved OMB No. 0704-0188	
Public reporting burden for the collection of information is estimated to average 1 hour per response, including the time for reviewing instructions, searching existing data sources, gathering and maintaining the data needed, and completing and reviewing the collection of information. Send comments regarding this burden estimate or any other aspect of this collection of information, including suggestions for reducing this burden, to Washington Headquarters Services, Directorate for Information Operations and Reports, 1215 Jefferson Davis Highway, Suite 1204, Arlington VA 22202-4302. Respondents should be aware that notwithstanding any other provision of law, no person shall be subject to a penalty for failing to comply with a collection of information if it does not display a currently valid OMB control number.				
1. REPORT DATE <b>2011</b>		2. REPORT TYPE		3. DATES COVERED <b>00-00-2011 to 00-00-2011</b>
4. TITLE AND SUBTITLE <b>Non-Equilibrium Green's Function Study of Transport in Disordered Double-Layer Graphene Systems</b>			5a. CONTRACT NUMBER	
			5b. GRANT NUMBER	
			5c. PROGRAM ELEMENT NUMBER	
6. AUTHOR(S)			5d. PROJECT NUMBER	
			5e. TASK NUMBER	
			5f. WORK UNIT NUMBER	
7. PERFORMING ORGANIZATION NAME(S) AND ADDRESS(ES) <b>University of Illinois at Urbana-Champaign,Electrical and Computer Engineering,Urbana,IL,61801</b>			8. PERFORMING ORGANIZATION REPORT NUMBER	
9. SPONSORING/MONITORING AGENCY NAME(S) AND ADDRESS(ES)			10. SPONSOR/MONITOR'S ACRONYM(S)	
			11. SPONSOR/MONITOR'S REPORT NUMBER(S)	
12. DISTRIBUTION/AVAILABILITY STATEMENT <b>Approved for public release; distribution unlimited</b>				
13. SUPPLEMENTARY NOTES				
14. ABSTRACT <b>The superfluid properties of disordered double-layer graphene systems are investigated using the non-equilibrium Green's function (NEGF) formalism. The complexity of such a structure makes it imperative to study the effects of lattice vacancies which will inevitably arise during fabrication. Room-temperature performance characteristics for both ideal and disordered bilayer graphene systems are compared in an effort to illustrate the behavior of a Bose-Einstein condensate in the presence of lattice defects under non-equilibrium conditions. The study finds that lattice vacancies that spread throughout the top layer past the coherence length have a reduced effect compared to the ideal case. However, vacancies concentrated near the metal contacts within the coherence length significantly alter the interlayer superfluid transport properties.</b>				
15. SUBJECT TERMS				
16. SECURITY CLASSIFICATION OF:			17. LIMITATION OF ABSTRACT <b>Same as Report (SAR)</b>	18. NUMBER OF PAGES <b>55</b>
a. REPORT <b>unclassified</b>	b. ABSTRACT <b>unclassified</b>	c. THIS PAGE <b>unclassified</b>		

NON-EQUILIBRIUM GREEN'S FUNCTION STUDY OF TRANSPORT IN  
DISORDERED DOUBLE-LAYER GRAPHENE SYSTEMS

BY

BRIAN JON DELLABETTA

THESIS

Submitted in partial fulfillment of the requirements  
for the degree of Master of Science in Electrical and Computer Engineering  
in the Graduate College of the  
University of Illinois at Urbana-Champaign, 2011

Urbana, Illinois

Adviser:

Assistant Professor Matthew J. Gilbert

# ABSTRACT

The superfluid properties of disordered double-layer graphene systems are investigated using the non-equilibrium Green's function (NEGF) formalism. The complexity of such a structure makes it imperative to study the effects of lattice vacancies which will inevitably arise during fabrication. Room-temperature performance characteristics for both ideal and disordered bilayer graphene systems are compared in an effort to illustrate the behavior of a Bose-Einstein condensate in the presence of lattice defects under non-equilibrium conditions. The study finds that lattice vacancies that spread throughout the top layer past the coherence length have a reduced effect compared to the ideal case. However, vacancies concentrated near the metal contacts within the coherence length significantly alter the interlayer superfluid transport properties.

# ACKNOWLEDGMENTS

I would like to thank my thesis adviser, Professor Matthew J. Gilbert, for his mentorship during my graduate studies. Prof. Gilbert has provided me with countless resources and conversations to expand my knowledge in this field as well as to network with top researchers at various conferences, domestic and international. His tireless efforts have allowed me not only to understand the research, but to see its usefulness and applicability in the real world and to consider many other interesting avenues to study.

I would also like to thank researchers at other institutions who have collaborated with us on this work. Professor Allan H. MacDonald (University of Texas-Austin) and Professor David Goldhaber-Gordon (Stanford University) and their respective research groups are collaborators on this particular project and have provided many useful insights in the realm of experimental realization.

Finally, I would like to thank my parents, whose love and support throughout my academic career has been invaluable.

This work was supported by the Army Research Office.

# TABLE OF CONTENTS

LIST OF ABBREVIATIONS . . . . .	v
CHAPTER 1 MOTIVATION . . . . .	1
CHAPTER 2 INTRODUCTION . . . . .	3
2.1 Superconductivity . . . . .	3
2.2 Bose-Einstein Condensation . . . . .	4
CHAPTER 3 TRANSPORT IN EXCITONIC SUPERFLUIDS . . . . .	6
3.1 Crossed Andreev Reflection . . . . .	6
3.2 Experimental Evidence . . . . .	8
CHAPTER 4 GRAPHENE . . . . .	11
4.1 Electronic Properties of Graphene . . . . .	11
4.2 Indirect Condensation in Double-Layer Graphene . . . . .	14
CHAPTER 5 NON-EQUILIBRIUM GREEN'S FUNCTION FORMAL-	
ISM . . . . .	16
5.1 Introduction . . . . .	16
5.2 Contact Self-Energies . . . . .	18
5.3 Retarded Green's Function . . . . .	19
5.4 Observables . . . . .	21
CHAPTER 6 ANALYSIS OF TRANSPORT IN SUPERFLUID DOUBLE-	
LAYER GRAPHENE . . . . .	22
6.1 Approach . . . . .	22
6.2 The Ideal System . . . . .	26
6.3 Disordered Systems . . . . .	31
6.3.1 Layer Disorder beyond $L_c$ . . . . .	33
6.3.2 Layer Disorder within $L_c$ . . . . .	37
CHAPTER 7 CONCLUSION . . . . .	42
REFERENCES . . . . .	44

# LIST OF ABBREVIATIONS

CMOS	Complementary Metal-Oxide-Semiconductor
MOSFET	Metal-Oxide-Semiconductor Field Effect Transistor
BCS	Bardeen-Cooper-Schrieffer (Theory of Superconductivity)
BEC	Bose-Einstein Condensation
NEGF	Non-Equilibrium Green's Function
RGF	Recursive Green's Function
QHE	Quantum Hall Effect
2DEG	2-Dimensional Electron Gas
BdG	Bogoliubov-de Gennes
LDOS	Localized Density of States

$E_F$	Fermi Energy
$v_F$	Fermi Velocity
$k_F$	Fermi Wave Vector
$T_c$	Critical Temperature
$\alpha$	Fine Structure Constant
$E_D$	Dirac Energy
$k_B$	Boltzmann's Constant
$\hbar$	Reduced Planck's Constant
$m_{exc}$	Complex Order Parameter, Superfluid Density
$\phi_{exc}$	Order Parameter Phase

$L_c$	Coherence Length
$\rho$	Density Matrix
$I_c$	Critical Interlayer (Tunneling) Current



# CHAPTER 1

## MOTIVATION

From high-performance parallel computing to hand-held devices, the advent of efficient computer processors has significantly changed the face of the technological landscape. The Internet has pervaded almost every facet of business information technology, from marketing to supply-chain management. None of this revolution would be possible without mobile and efficient data processing. Any computer or smart phone today is powered by complementary metal-oxide-semiconductor (CMOS) technology, which uses gated metal-oxide-semiconductor field effect transistors (MOSFETs) to implement Boolean logic gates to carry out any particular computation. For the better part of 40 years, the density and efficiency of these transistors has very closely followed Moore's law, which states the number of transistors in an integrated circuit doubles approximately every two years [1]. This is a remarkable trend propelled by decades of innovation in fabrication of silicon CMOS technology. The trend is expected to slow in subsequent years, however, as the transistor sizes and densities approach fundamental limits.

Perhaps the most insurmountable of these limits is the power density of current processors. Heat is generated when current flows through the doped silicon channel of a MOSFET. At low density, the heat can dissipate with simple air cooling techniques. Higher transistor densities, however, have begun to heat chips near the air cooling limit, at which point the processor would become too hot for normal operation and fails. At the same time, leakage current becomes a non-negligible factor in undesirable energy consumption as transistors shrink to dimensions where the effects of quantum tunneling through the gate oxide become apparent.

A large variety of devices have been proposed to overcome these inefficiencies. Three-dimensional gate structures were recently introduced in fabrication to increase channel mobility and decrease gate voltages in silicon channels. Gallium arsenide (GaAs) and other III-V channels provide an increase in electron mobility, decreasing power dissipation and the resultant heat generation. Organic electron-

ics, utilizing graphene or carbon nanotube (CNT) channels have more recently been studied due to their high carrier mobilities and thermal conductivity. Optoelectronic devices, using photons as signal carriers rather than electrons, are also being actively pursued and have found practical applications in large-scale data transfer utilizing optical fibers.

While this research has provided tremendous insight for solutions in the short run, the MOSFET's unavoidable limitations will remain a problem in any system with a semiconducting channel due to dissipation and scattering of individual carriers in the crystal lattice. A superconducting channel would resolve these issues, but to date no room-temperature superconducting system has been realized, and the channel cannot be turned on or off via a gate voltage. Recent work in condensed matter physics, however, has shown evidence of other condensed many-body systems that can flow around channel defects and impurities without dissipation or scattering losses in the same fashion as a superconductor. In Chapter 2, I describe this many-body phenomenon, known as Bose-Einstein condensation (BEC), and compare it to conventional superconductivity. I analyze its experimental realization in a variety of bosonic systems to elucidate how condensation starkly effects various macroscopic behaviors. In Chapter 3, I further discuss the realization of superfluid transport in coupled quantum well systems, and extend this idea in Chapter 4 to explain why double-layer graphene systems are a suitable candidate for room-temperature operation in which the superfluid can be switched on or off with a double-gate geometry. In Chapter 5, I provide a detailed summary of the non-equilibrium Green's function (NEGF) formalism and its ability to determine non-equilibrium transport dynamics of a system. In Chapter 6, I utilize NEGF to predict the observable behavior of the double-layer graphene system in both ideal and disordered systems in order to understand how imperfect graphene channels degrade transport dynamics.

# CHAPTER 2

## INTRODUCTION

### 2.1 Superconductivity

A boson is defined as any quasiparticle with integer spin. Bose first showed in 1925 that photons, spin-0 light quanta, adhere to statistics qualitatively different than fermions, particles with half-integer spin. Einstein subsequently extended Bose's study to matter to show that all integer-spin particles obey Bose-Einstein statistics, where the expected number of particles in a non-degenerate energy state  $i$  is

$$n_i = \frac{1}{e^{(E_i - \mu)/k_B T} - 1}, \quad (2.1)$$

where  $E_i$  is the energy of state  $i$ ,  $\mu$  is the chemical potential,  $T$  is the temperature and  $k_B$  is Boltzmann's constant. At energies well below the chemical potential, the expected number of particles becomes much larger than 1. This is in stark contrast to Fermi-Dirac statistics for fermions, or spin- $\frac{1}{2}$  particles like electrons and holes. The Pauli exclusion principle prevents fermions from occupying the same quantum state, limiting the expectation number to less than 1 for every fermion quantum state.

At low temperature, a large fraction of the bosons in a system decay to the lowest quantum state. Condensation in the lowest quantum state manifests itself with a variety of phenomena on the macroscopic scale, including superconductivity. The Bardeen-Cooper-Schrieffer (BCS) theory of superconductivity [2] was a crowning achievement of quantum mechanics in condensed matter systems. The discovery, now over fifty years old, explains superconductivity as the result of condensation of composite bosons into a ground state. BCS predicted, however, that two electrons can couple to form a composite boson quasiparticle called a Cooper pair. Electrons are repelled from one another by the Coulomb interaction, but at very low temperature a phonon-mediated electronic attraction can overcome the Coulomb repulsion. The resulting Cooper pair has an energy lower than the en-

ergy of a bare electron, and opens a gap about the Fermi energy,  $E_F$ . Cooper pairs are capable of flowing through the superconducting channel without dissipation, a macroscopic realization of the many-body coherence. The pairing is very weak, however, and superconductivity is quickly lost as temperature increases above the critical temperature  $T_c$  - the temperature at which phonons, vibrations in the crystal lattice, dominate electron motion and annihilate the weak Cooper pairs.

While the discovery of superconductivity has bred a wealth of research into high  $T_c$  unconventional superconductors, whose critical temperatures approach 150 K [3],  $T_c$  remains well below room temperature due to the long-range phonon-mediated nature of the condensation. However, if a strong Coulomb attraction between oppositely charged particles replaced the weak attraction in superconductivity, the bosons could condense and survive at much higher temperatures. In the following section, I will describe such an interaction and show how the pairing can be large enough to remain condensed at room temperature.

## 2.2 Bose-Einstein Condensation

Although BEC was first predicted in the 1920s, experimental realization did not occur until 1995 with a gas of weakly interacting rubidium atoms cooled to nearly 20 nK [4]. Anderson et al. found a signature of BEC when the concentration of rubidium atoms in the zero-velocity ground state increased abruptly as the sample was lowered below the critical temperature, which for a three-dimensional non-interacting gas is

$$T_c = \frac{2\pi\hbar^2}{m_{Rb}k_B} \left( \frac{n}{\zeta(3/2)} \right)^{2/3} \approx 50 \text{ nK}. \quad (2.2)$$

where  $m_{Rb}$  is the mass of a rubidium atom,  $n$  is the number of particles in the system, and  $\zeta$  is the Riemann zeta function.

While the rubidium atom experiment provided definitive evidence of BEC, a sub-micro Kelvin critical temperature is of little practical value. However, this realization is in the weakly interacting regime with very heavy atoms (note that critical temperature is inversely proportional to mass in Eq. 2.2). Subsequent research has shown that condensates can be formed with weakly interacting exciton-polariton quasiparticles, which are created with a continuous wave photo-pump in a semiconductor cavity. As long as the polariton generation rate is larger than the

rate at which the quasiparticles recombine, a condensate can persist. Exciton-polariton quasiparticles have effective masses  $10^9$  times lighter than rubidium atoms, so that they are suitable for observed condensation at 19 K [5; 6]. Further research has shown that polaritons with even smaller effective masses can have critical temperatures above room temperature in pristine bulk GaN microcavities [7; 8].

Polariton condensates provide a unique environment to observe various signatures of BEC. The most important of these for the scope of this thesis is dissipationless flow, or zero viscosity, known as superfluidity. The BEC is a superfluid state, meaning it can flow freely and without diffusion through a system in the same way a Cooper pair flows freely through a superconducting channel. The best known observation of this is the ability of superfluid  $\text{He}^4$  to escape out of a container by flowing along the walls of the container [9]. In a similar fashion, Amo et al. [10] showed that droplets of polariton condensation can be excited to flow through the channel in which they are formed with a simple light pulse. The droplets move with a constant high group velocity, roughly  $1.0 \times 10^6$  m/s, and are able to move around defects without scattering. When the polariton superfluid reaches a defect with size comparable to its own, it tends to split the superfluid into two droplets, but phase coherence is not lost and group velocity remains unperturbed. Although the exciton-polariton is charge neutral, the observed transport dynamics offer strong insight to the technological ramifications of superfluid transport - macroscopic coherence that precludes diffusion from material defects. In the next section, I will describe a system in which charge can be separately transferred in a excitonic superfluid system, as well as experimental realization in the quantum Hall regime.

# CHAPTER 3

## TRANSPORT IN EXCITONIC SUPERFLUIDS

### 3.1 Crossed Andreev Reflection

From a theoretical standpoint, an indirectly bound exciton superfluid can form when two channels are stacked in close proximity to one another and doped so that a large number of electrons (holes) occupy the top (bottom) layer. The carriers in the top layer will form indirect excitons (bosons) with holes in the bottom layer via an interlayer Coulomb interaction, but are prevented from recombining by a small spacer dielectric. This is analogous to the polariton condensates discussed in the previous section, with the exception that photo-pumping is not necessary for condensation, and the constituent components of the condensate are separately contacted.

It is vital to first understand the transport properties that can be achieved in such an indirectly bound excitonic superfluid system. To obtain a more in-depth understanding of the interlayer transport in double-layer graphene systems, I first draw a comparison to the Andreev reflections [12] that occur at a metal-superconductor interface. When an electron with energy less than the superconducting band gap is injected into a superconducting system, the injected electron penetrates a certain distance before propelling a Cooper pair across the superconducting channel, as seen in Fig. 3.1a. A hole of opposite spin is retro-reflected back into the metal contact to conserve momentum. Similar physics occur when an electron with energy less than the superfluid band gap is injected into the excitonic superfluid channel. Figure 3.1b shows that the injected electron will penetrate a short distance in the top layer before driving an exciton that moves across the channel. This process corresponds to an electron being injected into the top left contact that causes an exciton to move across the system while an electron is reflected into the bottom left contact to conserve current [11]. The injected and retro-reflected currents are separated in the top left and bottom left contacts, and the resulting physics is

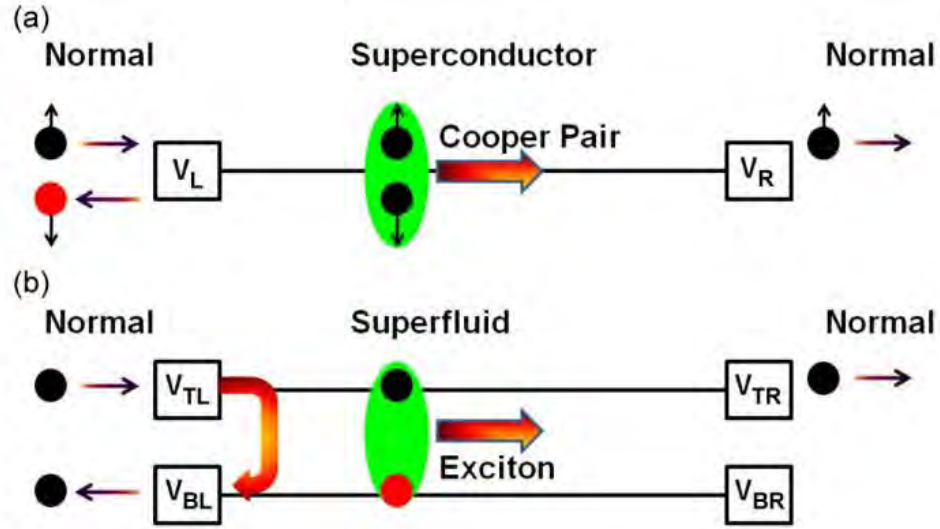


Figure 3.1: (a) Depiction of Andreev reflection in metal-superconductor-metal system. Non-equilibrium contact bias will inject an electron of a certain spin (black dot) into the system from the left contact. The action will cause a Cooper pair to flow along the channel, resulting in a single electron coming out of the right contact and a hole (red dot) of opposite spin from the left contact to conserve momentum. (b) Depiction of crossed Andreev reflection in an indirectly bound exciton superfluid. When an electron is injected in the top left contact in non-equilibrium, an exciton will be driven along the channel, resulting in an electron coming out of the top right contact and bottom left contact to conserve momentum. Image from [11].

termed crossed Andreev reflection.

The drag-counterflow geometry ( $V_{TL} = -V_{TR}$ ;  $V_{BL} = V_{BR} = 0$  V) will cause an electron to be reflected into the bottom left contact and a hole into the bottom right contact [13], inducing an effective current through the bottom layer only when a condensate exists. All non-equilibrium configurations described below are in this geometry. The entire process results in a condensate current, due to the propagating exciton, and a quasiparticle current, caused by the injected and retro-reflected individual carriers. The quasiparticle current is only nonzero within the coherence length ( $L_c$ ), which is the maximum length an injected particle penetrates into the superfluid gap before triggering the exciton scattering event. While the microscopic attributes of the superfluid and the dynamics of the Andreev reflection may not be readily apparent in experiments, they will have a macroscopic effect on the observable interlayer current. The next section will discuss the realization of such a system using coupled quantum wells in the quantum Hall regime.

## 3.2 Experimental Evidence

The quantum Hall effect (QHE), first shown experimentally in 1980 [14], was a landmark discovery in condensed matter physics for its ability to determine the fine-structure constant,  $\alpha$ , and the quantum of conductance with high precision. In the QHE, a strong magnetic field of 15 T is applied perpendicularly to a pristine semiconductor quantum well which can be treated as a 2-dimensional electron gas (2DEG). At extremely low temperatures, the magnetic field dominates the electron dynamics so that electrons occupy quantized cyclotron orbits known as Landau levels with cyclotron frequency  $\omega_c = qB/m$ , where  $B$  is magnetic field strength,  $q$  is the charge of the electron, and  $m$  is its effective mass. Electrons in each Landau level have discrete energy values,

$$E_n = \hbar\omega_c(n + \frac{1}{2}), \quad (3.1)$$

which are analogous to the quantum harmonic oscillator. At weak magnetic fields, Landau quantization is responsible for Shubnikov-de Haas oscillations, a well-known relation in which the longitudinal resistance oscillates as the magnetic field is modulated. Stronger magnetic fields further separate the discrete Landau energies, and as more Landau levels are pushed above  $E_F$ , the Hall conductivity



decreases according to

$$\sigma_{xy} = \nu \frac{q^2}{h}, \quad (3.2)$$

where  $\nu$  is the number of Landau levels below  $E_F$ . This is due to the fact that only edge states are available for transport in the quantum Hall regime; longitudinal transport is prevented by the confining magnetic field unless a Landau level is crossing  $E_F$ . The QHE thus shows that conductance, like so many other physical observables, takes on a quantized value proportional to some integer times the quantum of conductance,  $q^2/h$ , and the number of filled Landau levels can be extracted easily from the conductance. It is important to note that conductance does not depend on semiconductor material or length because carrier edge states are completely protected from backscattering in the quantum Hall regime.

In recent years, significant experimental [15–18] and theoretical [19–23] progress has been made in the search for BEC in coupled quantum wells in the quantum Hall regime. Consider two GaAs quantum wells separated by a thin insulating barrier layer. When the individual filling factor of each 2DEG is tuned to  $\nu = 1/2$ , so that the total filling factor is  $\nu_{total} = 1$ , the density of electrons and holes in the lowest Landau level is equivalent. The system thus develops a spontaneous interlayer phase coherence when the separation between the two layers is small enough to allow interlayer Coulomb pairing, which occurs at less than roughly 10 nm [24]. The holes (electrons) in one layer form indirect excitons with the electrons (holes) in the opposite layer. The layer separation greatly increases exciton lifetimes, which otherwise would be too small for conventional excitonic condensation in bulk semiconductors [25] because the electron and hole are not hindered from immediately recombining. Thus the layer separation is finely tuned so that it is small enough for Coulomb attraction and exciton formation but large enough to prevent tunneling and recombination.

The indirect excitons, being composite bosons, form a BEC in the same fashion as the rubidium atoms and exciton-polaritons. When carriers are injected into one of the two 2DEGs, excitons in the condensate are propagated along the channel, the physics of which is known as Andreev reflection and is discussed at length in Section 3.1. Thus a current can be observed in the opposite layer in spite of a bottom layer contact bias. This is known as resonant tunneling current, which peaks at a filling factor of exactly one-half [26]. Tunneling current is linearly proportional to the total current in the system. Critical tunneling current, the maximum attainable current in the BEC phase, was observed to be 1.5 nA [27] before the

condensate is destroyed by the influx of individual quasiparticles, at which point tunneling becomes negligible.

Critical current is extremely sensitive to filling factor, and quickly drops to a negligible amount when total filling factor is below 0.9 or above 1.1 [28]. This lends credence to the theory that a BEC can only form in a coupled quantum well system when electron and hole quasiparticle densities are equivalent in each layer. Inequalities in the quasiparticle concentrations hinder exciton formation by screening out interlayer interaction. The resonant tunneling phenomenon is lost at temperatures outside of the quantum Hall regime [26]. Although the critical temperature for excitonic condensation is high, equal carrier concentrations can only be achieved in the quantum Hall regime, which requires sub-Kelvin temperatures and magnetic fields on the order of 10 T. Recent theoretical studies, however, have predicted this can be resolved by replacing the coupled semiconductor quantum well heterostructure with a double-layer graphene system. In the next section, I will analyze carrier transport in graphene and show how its properties make it an ideal candidate for indirectly bound excitonic condensation with critical temperatures approaching room temperature.

# CHAPTER 4

## GRAPHENE

### 4.1 Electronic Properties of Graphene

The unique electronic properties of graphene - an individual sheet of graphite - were first predicted in 1946, long before its experimental discovery [29]. Figure 4.1 shows a top-down view of the hexagonal arrangement of the carbon atoms in real space in the graphene sheet as well as the first Brillouin zone in reciprocal space. The basis vectors are

$$\begin{aligned}\vec{a}_1 &= |a_0| \left( \frac{\sqrt{3}}{2} \hat{x} + \frac{1}{2} \hat{y} \right) \\ \vec{a}_2 &= |a_0| \left( \frac{\sqrt{3}}{2} \hat{x} - \frac{1}{2} \hat{y} \right),\end{aligned}\tag{4.1}$$

where the magnitude of the basis vectors is  $|a_0| = \sqrt{3}a_{cc}$ . The distance between nearest neighbor carbon atoms is  $a_{cc} \approx 0.142$  nm.

In order to calculate the band structure of graphene, a tight binding model is used in which a single  $p_z$  orbital per carbon atom interacts with nearest neighbor sites. This approximation works well at low energies near the Fermi energy; which is the only important energy range for electrical conduction, because other orbitals are either well above or well below  $E_F$ . The 2x2 Hamiltonian can thus be written in reciprocal space by summing over any unit cell and its six neighboring unit cells,

$$H(\vec{k}) = -\tau \begin{bmatrix} 0 & 1 + e^{i\vec{k} \cdot \vec{a}_1} + e^{i\vec{k} \cdot \vec{a}_2} + e^{i\vec{k} \cdot \vec{a}_3} \\ 1 + e^{-i\vec{k} \cdot \vec{a}_1} + e^{-i\vec{k} \cdot \vec{a}_2} + e^{-i\vec{k} \cdot \vec{a}_3} & 0 \end{bmatrix},\tag{4.2}$$

where  $\tau = -3.03$  eV is the bonding energy between carbon atoms and  $\vec{a}_3 = \vec{a}_1 - \vec{a}_2 = a_0 \hat{y}$ . The dispersion relation,  $E(\vec{k})$ , can be calculated by solving for the eigenvalues

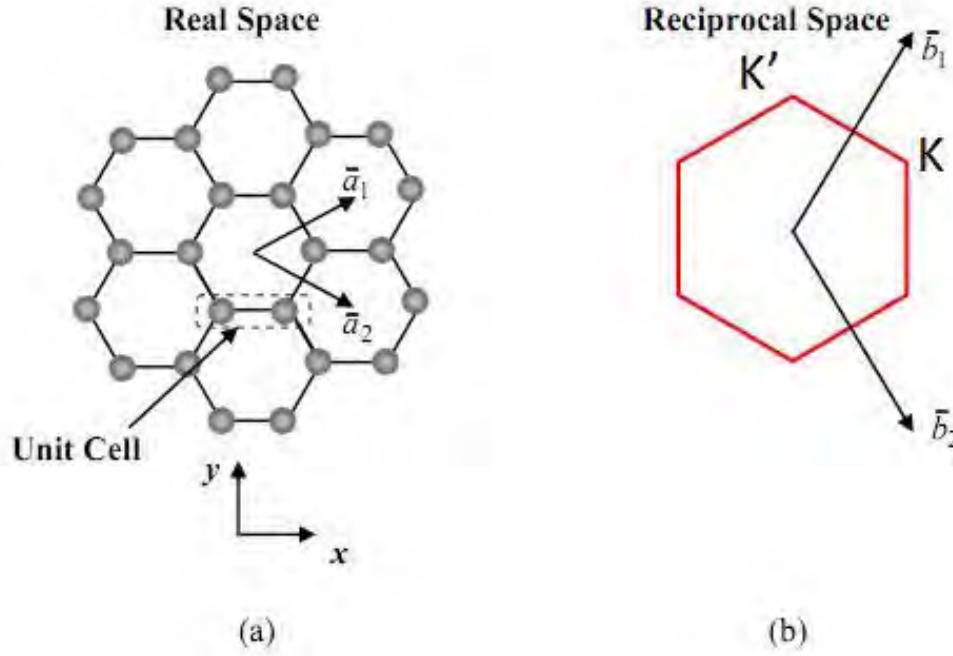


Figure 4.1: (a) Real space depiction of a graphene lattice. The unit cell encompasses two carbon atoms, with basis vectors  $\vec{a}_1$  and  $\vec{a}_2$ . (b) The first Brillouin zone of graphene in reciprocal space, with basis vectors  $\vec{b}_1$  and  $\vec{b}_2$ . The K and K' points in the Brillouin zone are responsible for massless transport at low energy. Adapted from [30].

of Eq. 4.2,

$$E(\vec{k}) = \pm t \sqrt{3 + 2 \cos \vec{k} \cdot \vec{a}_1 + 2 \cos \vec{k} \cdot \vec{a}_2 + 2 \cos \vec{k} \cdot \vec{a}_3}, \quad (4.3)$$

where positive (negative) energies denote the conduction (valence) bands for the graphene lattice. Graphene is thus particle-hole symmetric about  $E_F$ , an important property which will be exploited in Section 4.2 to get the equivalent quasiparticle densities necessary for exciton condensation. This property is in stark contrast to silicon and other bulk semiconductors, which have conduction band minima and valence band maxima that do not lie at the same energy or wave vector and are not particle-hole symmetric.

The basis vectors in reciprocal space must, for any system, satisfy

$$\vec{a}_i \cdot \vec{b}_j = 2\pi\delta_{ij}, \quad (4.4)$$

where  $\delta_{ij}$  is the Kronecker delta. For graphene, the reciprocal space basis vectors are

$$\begin{aligned} \vec{b}_1 &= \frac{4\pi}{a_0\sqrt{3}} \left( \frac{1}{2}\hat{x} + \frac{\sqrt{3}}{2}\hat{y} \right) \\ \vec{b}_2 &= \frac{4\pi}{a_0\sqrt{3}} \left( \frac{1}{2}\hat{x} - \frac{\sqrt{3}}{2}\hat{y} \right) \end{aligned} \quad (4.5)$$

to satisfy Equations 4.1 and 4.4. The K and K' valleys of the Brillouin zone, shown in Fig. 4.1b, are located at wave vector

$$\vec{k}_K = (n \pm \frac{1}{3})\vec{b}_1 + (m \mp \frac{1}{3})\vec{b}_2, \quad n, m \in \mathbb{Z} \quad (4.6)$$

where  $n$  and  $m$  are integers. When  $\vec{k}_K$  is plugged into the dispersion relation equation, the energy vanishes,

$$E(\vec{k}_K) = \pm t \sqrt{3 + 2 \cos \pm \frac{2}{3}\pi + 2 \cos \mp \frac{2}{3}\pi + 2 \cos \pm \frac{4}{3}\pi} = 0. \quad (4.7)$$

When solved numerically,  $E(\vec{k})$  follows a linear dispersion about each K/K' point of the Brillouin zone, as seen in Fig. 4.2. The linear dispersion is symmetric about the Dirac point,  $E_D$ , in the approximate energy range of  $E_D \pm 1$  eV. The Fermi velocity is constant in the linear regime and proportional to the slope of the dispersion,

$$v_F = \frac{1}{\hbar} \frac{\partial E}{\partial k} \approx 10^6 \text{ m/s}, \quad (4.8)$$

which is roughly 1/300 the speed of light in a vacuum. The linear band structure means that carriers act as massless Dirac fermions in graphene, because effective mass is proportional to  $\partial^2 E / \partial k^2$ .

The electrical properties of graphene are thus unique and quite remarkable. Unlike as in any semiconducting material, electron and hole quasiparticles are able to flow in bulk graphene at equivalent velocities due to their equivalent mobilities. For this reason, graphene has become an area of immense study since its initial experimental discovery [31]. Proof of the high carrier mobility was seen from observation of the QHE in graphene at room temperature [32]. The predicted

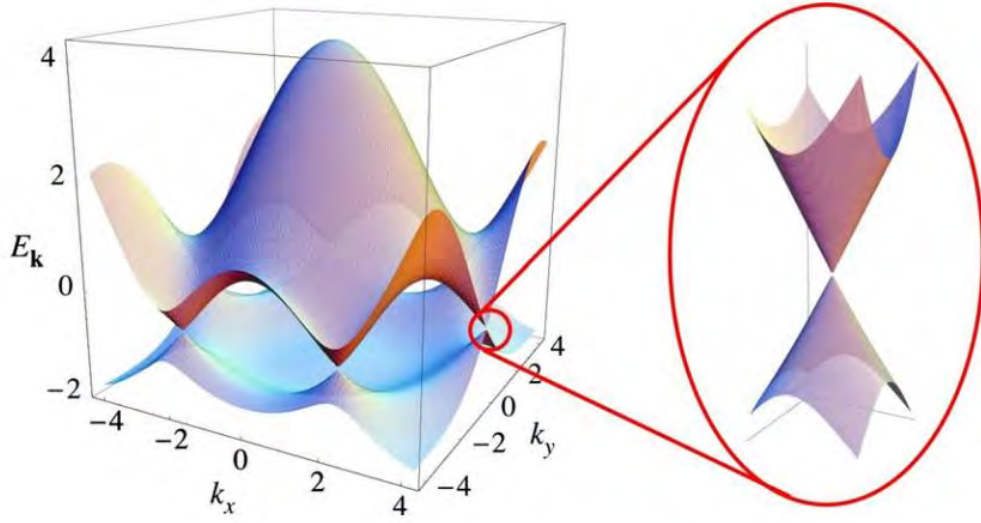


Figure 4.2: The dispersion relation,  $E(\vec{k})$ , of graphene is isotropic and linear at low energy. Zero energy modes exist at the K and K' points of the Brillouin zone. There are a total of six such points in the first Brillouin zone, but only two are independent. Image from [33].

Fermi velocity,  $v_F$ , is extremely high, and allows pristine graphene samples to have equivalent room temperature carrier mobilities of  $2 \times 10^5 \text{ cm}^2\text{V}^{-1}\text{s}^{-1}$ , several orders higher than bulk silicon ( $\leq 1400 \text{ cm}^2\text{V}^{-1}\text{s}^{-1}$  [34]). In Section 4.2, it is shown that these properties make graphene an ideal choice for double-layer excitonic superfluidity. Unfortunately, efficient graphene growth has proven difficult, and the best large-scale synthesis techniques, performed by epitaxial growth on copper foils, yield carrier mobilities several orders smaller than the best samples [35]. As such, disorder in the graphene channel becomes an important factor in superfluid transport, and is discussed in the superfluid regime in Section 6.3.

## 4.2 Indirect Condensation in Double-Layer Graphene

In Chapter 3, it is shown that a BEC can arise in coupled quantum well systems in the quantum Hall regime when each layer has a filling factor of  $\nu = \frac{1}{2}$ . The quantum Hall regime is necessary for particle-hole symmetry about the Fermi energy, so that each layer has an equivalent quasiparticle density. The system is not suited for room-temperature application because the QHE requires very large and

precise magnetic fields and very low temperatures. However, recent theoretical studies [36; 37] have predicted the the same effect is possible in spatially separated monolayers of graphene, as depicted in Fig. 4.3. Mean-field calculations have shown that, when the two monolayers are separated by a  $\text{SiO}_2$  spacer dielectric on the order of 1 nm thick and the Fermi energy of the top (bottom) monolayer is gated to  $E_D + 0.4$  eV ( $E_D - 0.4$  eV),  $T_c$  can approach room temperature [38]. In the next chapter, I will explain the NEGF formalism which is implemented to study the transport dynamics of the double-layer graphene system.

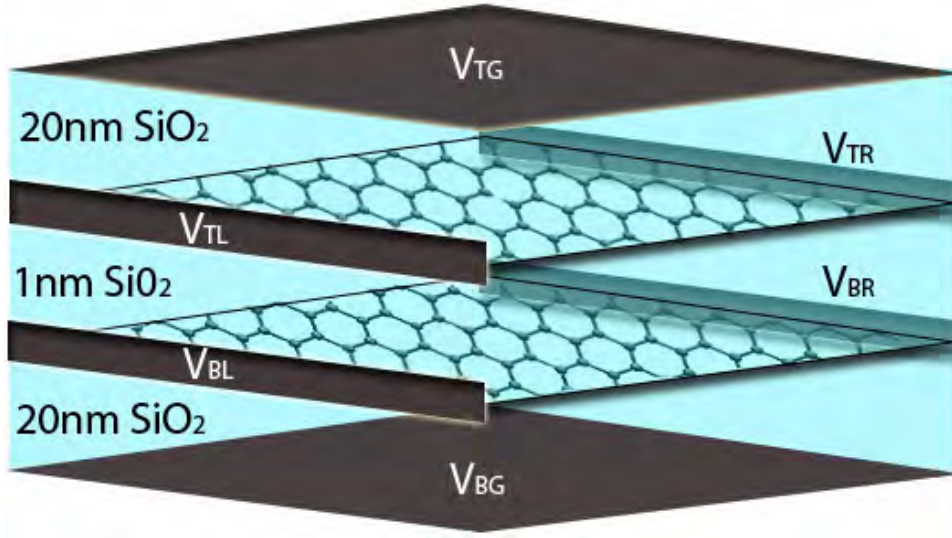


Figure 4.3: Schematic depiction of the double-layer graphene system. A 1 nm  $\text{SiO}_2$  dielectric separates the two graphene monolayers, whose Fermi levels are set to  $\pm 0.4$  eV by the top and bottom gates,  $V_{TG}$  and  $V_{BG}$ , to effect equivalent but oppositely charged quasiparticle densities in each layer. Four contacts on either side of the monolayers are responsible for inducing a counterflow current.

# CHAPTER 5

## NON-EQUILIBRIUM GREEN'S FUNCTION FORMALISM

### 5.1 Introduction

Figure 5.1 shows a generic system to be simulated with NEGF [39; 40]. The electron dynamics of the channel are completely described by its Hamiltonian,  $\mathbf{H}$ , which is connected to two contact reservoirs with respective chemical potential  $\mu_L$  and  $\mu_R$ . Contacts couple to the channel via self-energy matrices,  $\Sigma_L$  and  $\Sigma_R$ , which will be defined in Section 5.2, to induce a non-equilibrium current flow. The simulation assumes ballistic transport, so self-energy from scattering,  $\Sigma_S$ , is neglected. The system is insulated from gate contacts, whose effects are realized via a three-dimensional Poisson solver, which solves for the potential at a given point in real space based on the electron density,

$$\nabla^2 \phi(\vec{r}) = \frac{q^2}{\epsilon} [N_D(\vec{r}) - n(\vec{r})], \quad (5.1)$$

where  $\phi(\vec{r})$  is the potential profile and  $N_D(\vec{r})$  is the carrier density from donors, which is nonzero only for doped semiconductors. The electron density,  $n(\vec{r})$ , is evaluated in the NEGF kernel (see Eq. 5.15), thus the NEGF and Poisson algorithms must be repeated until a self-consistent solution is achieved. The system is easily expandable to systems with several contacts or gate configurations by adding additional self-energy matrices to NEGF or additional sources to the Poisson solver. In the case of Fig. 4.3, there are four contacts connected to the system and two gates electrostatically dope the monolayers.

The channel is defined to be three-dimensional in nature, with  $N_x$ ,  $N_y$ , and  $N_z$  lattice points in the x, y, and z directions. The full three-dimensional real space Hamiltonian matrix can be written in terms of its directional hopping amplitudes



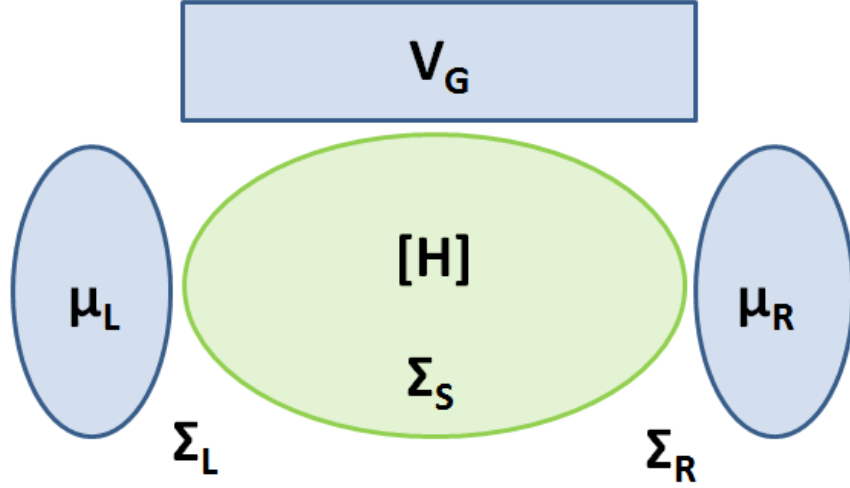


Figure 5.1: A generalized NEGF system. Two contacts with chemical potentials  $\mu_L$  and  $\mu_R$  place the system with Hamiltonian  $H$  in a non-equilibrium state to induce current flow. An assortment of gates with potential  $V_G$  electrostatically dopes the system according to the Poisson equation.

in the following nested block tridiagonal structure,

$$\mathbf{H} = \begin{bmatrix} \mathbf{H}_0 & \mathbf{H}_1 & 0 & \cdots & 0 & 0 \\ \mathbf{H}_1^\dagger & \mathbf{H}_0 & \mathbf{H}_1 & 0 & \cdots & 0 \\ 0 & \mathbf{H}_1^\dagger & \mathbf{H}_0 & \mathbf{H}_1 & 0 & \cdots & \vdots \\ \vdots & 0 & \ddots & \ddots & \ddots & 0 & \\ & \vdots & & \ddots & \ddots & \ddots & 0 \\ 0 & 0 & \cdots & \ddots & \mathbf{H}_1^\dagger & \mathbf{H}_0 & \mathbf{H}_1 \\ 0 & 0 & & \cdots & 0 & \mathbf{H}_1^\dagger & \mathbf{H}_0 \end{bmatrix}. \quad (5.2)$$

In Equation 5.2,  $\mathbf{H}_1 = [\mathbb{I}_{(N_x N_y)} \otimes \text{Hop}_Z]$  where  $\mathbb{I}_{(N_x N_y)}$  is the identity matrix of dimension  $N_x N_y$ ,  $\text{Hop}_Z$  is the hopping amplitude in the  $z$  direction, and  $\otimes$  is the Kronecker product. The on-diagonal component is itself a nested block

tridiagonal matrix,

$$\mathbf{H}_0 = \begin{bmatrix} \mathbf{H}_{00} & \mathbf{H}_{01} & 0 & \cdots & & 0 & 0 \\ \mathbf{H}_{01}^\dagger & \mathbf{H}_{00} & \mathbf{H}_{01} & 0 & \cdots & & 0 \\ 0 & \mathbf{H}_{01}^\dagger & \mathbf{H}_{00} & \mathbf{H}_{01} & 0 & \cdots & \vdots \\ \vdots & 0 & \ddots & \ddots & \ddots & 0 & \\ & \vdots & & \ddots & \ddots & \ddots & 0 \\ 0 & 0 & \cdots & \ddots & \mathbf{H}_{01}^\dagger & \mathbf{H}_{00} & \mathbf{H}_{01} \\ 0 & 0 & & \cdots & 0 & \mathbf{H}_{01}^\dagger & \mathbf{H}_{00} \end{bmatrix}. \quad (5.3)$$

The nested matrix  $H_0$  similarly has components  $\mathbf{H}_{01} = [\mathbb{I}_{(N_y)} \otimes Hop_X]$  and

$$\mathbf{H}_{00} = \begin{bmatrix} AA & Hop_Y & 0 & \cdots & & 0 & 0 \\ Hop_Y^\dagger & AA & Hop_Y & 0 & \cdots & & 0 \\ 0 & Hop_Y^\dagger & AA & Hop_Y & 0 & \cdots & \vdots \\ \vdots & 0 & \ddots & \ddots & \ddots & 0 & \\ & \vdots & & \ddots & \ddots & \ddots & 0 \\ 0 & 0 & \cdots & \ddots & Hop_Y^\dagger & AA & Hop_Y \\ 0 & 0 & & \cdots & 0 & Hop_Y^\dagger & AA \end{bmatrix}. \quad (5.4)$$

Note that  $\mathbf{H}$  and  $\mathbf{H}_0$  are block tridiagonal, but  $\mathbf{H}_{00}$  is not when periodic boundary conditions in  $y$  are used.

## 5.2 Contact Self-Energies

The channel is only connected to the contacts along the width at  $x = 1$  and  $x = N_x$ , for various points in  $z$ , so that the self-energy matrices of the left and right contacts,  $\Sigma_1$  and  $\Sigma_2$ , have a nonzero component dimension of  $N_y \times N_y$ . The full self-energy matrix has dimensions equivalent to the full Hamiltonian, but is zero at all points not connected to the lead. The contacts are assumed to be semi-infinite so that the surface Green's function,  $\mathbf{g}_L^s$ , self-consistently satisfies the relation

$$\mathbf{g}_L^s(E) = [(E + i0^+) \mathbb{I}_{(N_y)} - \mathbf{H}_{00} + \mathbf{H}_{01}^\dagger \mathbf{g}_L^s \mathbf{H}_{01}]. \quad (5.5)$$

The nonzero component of the self-energy matrix can then be computed as

$$\Sigma_1(E) = \mathbf{H}_{01}^\dagger \mathbf{g}_L^s(E) \mathbf{H}_{01}. \quad (5.6)$$

$\Sigma_2(E)$  can be calculated in the same fashion; the nonzero components of the self-energies are equivalent in this particular case. The imaginary part of the self-energy matrix is the energy level broadening due to the contact,

$$\Gamma_1 = \frac{i}{2}(\Sigma_1 - \Sigma_1^\dagger), \quad (5.7)$$

which represents the rate at which carriers are injected into the channel for each lattice point connected to the leads. The broadening matrices become important in subsequent sections when calculating transport dynamics of the system.

### 5.3 Retarded Green's Function

Given these definitions, the retarded Green's function can be computed as

$$\mathbf{G}^R(E) = [(E + i0^+) \mathbb{I}_{(N_x N_y N_z)} - \mathbf{H} - \Sigma_L - \Sigma_R]^{-1}. \quad (5.8)$$

This quickly becomes intractable for large system sizes, but the sparse, block tridiagonal structure of the Hamiltonian (see Equations 5.2 and 5.3) can be exploited to convert the  $O((N_x N_y N_z)^3)$  inversion computation to  $O(N_x N_y N_z)$  using the recursive Green's function (RGF) method. The matrix to be inverted has the following block tridiagonal structure:

$$\mathbf{G}^R(E) = \begin{bmatrix} \mathbf{D}_0 & \mathbf{t}_{0,1} & & & & & \\ \mathbf{t}_{1,0} & \mathbf{D}_1 & \mathbf{t}_{1,2} & & & & \\ & \mathbf{t}_{2,1} & \mathbf{D}_2 & \mathbf{t}_{2,3} & & & \\ & & & \ddots & \ddots & \ddots & \\ & & & & \ddots & \ddots & \\ & & & & & \mathbf{t}_{N-2,N-3} & \mathbf{D}_{N-2} & \mathbf{t}_{N-2,N-1} \\ & & & & & & \mathbf{t}_{N-1,N-2} & \mathbf{D}_{N-1} \end{bmatrix}^{-1}. \quad (5.9)$$

The recursive routine involves a forward and backward recursive sweep. For the forward sweep, I define a new set of matrices,

$$\begin{aligned} \mathbf{g}_{0,0}^{LR} &= (\mathbf{D}_0)^{-1} \\ \mathbf{g}_{i,i}^{LR} &= (\mathbf{D}_i - \mathbf{t}_{i,i-1} \mathbf{g}_{i-1,i-1}^{LR} \mathbf{t}_{i-1,i})^{-1}, i \in 1, 2 \dots N-1. \end{aligned} \quad (5.10)$$

The backward recursion yields the on-diagonal blocks of the retarded Green's function,

$$\begin{aligned} \mathbf{G}_{N-1,N-1}^R &= \mathbf{g}_{N-1,N-1}^{LR} \\ \mathbf{G}_{i,i}^R &= \mathbf{g}_{i,i}^{LR} (\mathbb{I} + \mathbf{t}_{i,i+1} \mathbf{G}_{i+1,i+1}^R \mathbf{t}_{i+1,i} \mathbf{g}_{i,i}^{LR}), i \in N-2, N-3 \dots 1, 0, \end{aligned} \quad (5.11)$$

where  $\mathbb{I}$  is the identity matrix of equivalent size. The off-diagonal blocks are

$$\mathbf{G}_{i,j}^R = \begin{cases} -\mathbf{g}_{i,i}^{LR} \mathbf{t}_{i,i+1} \mathbf{G}_{i+1,j}^R, & i < j \\ -\mathbf{g}_{j,j}^{LR} \mathbf{t}_{j,j+1} \mathbf{G}_{j+1,i}^R, & i > j \end{cases}. \quad (5.12)$$

The entire matrix can thus be resolved with the recursive algorithm. The blocks to be inverted are block tridiagonal themselves, so that the algorithm can be used in a recursive fashion within itself. The resulting complexity of the computation is  $O(N_x N_y N_z)$ .

The electron and hole correlations are given by

$$\begin{aligned} \mathbf{G}^n(E) &= \mathbf{G}^R [f_L \mathbf{\Gamma}_L + f_R \mathbf{\Gamma}_R] (\mathbf{G}^R)^\dagger \\ \mathbf{G}^p(E) &= \mathbf{G}^R [(1 - f_L) \mathbf{\Gamma}_L + (1 - f_R) \mathbf{\Gamma}_R] (\mathbf{G}^R)^\dagger, \end{aligned} \quad (5.13)$$

where  $f_L$ , dependent on the contact chemical potential,  $\mu_L$ , is given by the Fermi-Dirac distribution,

$$f_L(E) = \frac{1}{e^{(E - \mu_L)/kT} + 1}. \quad (5.14)$$

## 5.4 Observables

All desirable results can be calculated from the electron and hole correlated Green's functions. These include the following:

$$\begin{aligned}
T_{LR}(E) &= \text{Tr}(\mathbf{\Gamma}_L \mathbf{G}^R \mathbf{\Gamma}_R (\mathbf{G}^R)^\dagger) \\
I_{LR} &= \frac{e^2}{h} \int_{-\infty}^{\infty} T_{LR}(E) [f_L(E) - f_R(E)] dE \\
\rho_{i,j} &= e \int_{-\infty}^{\infty} \frac{dE}{2\pi} \mathbf{G}_{i,j}^n(E).
\end{aligned} \tag{5.15}$$

$T_{LR}$  denotes transmission from left to right contacts, and current  $I_{LR}$  is the integral over the transmission for which the Fermi-Dirac distributions of the contacts are unequal. The spatially resolved electron density,  $\rho_{i,j}$ , is an integral over the electron correlated Green's function, which is used in the Poisson solver to achieve a self-consistent solution. Hole density is the same integral over the hole correlated Green's function, so that the sum of the two at any on-diagonal point is the localized density of states for the particular lattice/orbital.

The current can likewise be resolved spatially, so that the total current from any point to any other point on the lattice is

$$\begin{aligned}
I_{j \rightarrow j+1} &= \frac{ie}{h} \int \frac{dE}{2\pi} [H_{j,j+1} G_{j+1,j}^n(E) - H_{j+1,j} G_{j,j+1}^n(E) \\
&\quad - H_{j,j+1} G_{j+1,j}^p(E) + H_{j+1,j} G_{j,j+1}^p(E)].
\end{aligned} \tag{5.16}$$

In the case of graphene, the Hamiltonian is only nonzero for nearest neighbors, so  $j+1$  denotes a lattice point that is only one point away from  $j$  in any direction. All elements in Eq. 5.16 are scalars because one orbital sufficiently describes each lattice point. The total current between lattice points is thus an integral of scalar values rather than an integral sum over matrices.

As a verification, the sum of all longitudinal current over any slice in the y-z plane is constant for any point in x and equivalent to  $I_{LR}$ . All matrix elements are verified for small system sizes using conventional matrix inversion/multiplication methods to ensure the validity of the RGF algorithm.

# CHAPTER 6

## ANALYSIS OF TRANSPORT IN SUPERFLUID DOUBLE-LAYER GRAPHENE

### 6.1 Approach

The system of interest is depicted in Fig. 4.3. This thesis studies two electrostatically doped zigzag graphene monolayers that are assumed to be perfectly registered with one another and separated by a thin dielectric. Contacts along the edges of each of the layers inject and extract current, and top and bottom gates manipulate the quasiparticle concentrations in each of the layers. In this way, the proper quasiparticle concentrations predicted by many-body theory [38] may be tuned to induce a superfluid phase transition. The top and bottom gates are separated from the graphene layers by 20 nm of  $\text{SiO}_2$ . The two graphene layers are separated from one another by a 1 nm  $\text{SiO}_2$  spacer dielectric to be in the predicted regime of superfluidity. The oxide regions are assumed to be perfect in the sense that they do not contain any stray charges and have perfect interfaces with the graphene layers. I choose the  $\hat{x}$  direction to lie along the length of the system, the  $\hat{y}$  direction to lie along the width, and the  $\hat{z}$  direction along the depth. Each monolayer is 30 nm long by 10 nm wide. These dimensions were selected rather than larger system sizes so that the atomistic transport properties of an increased number of disorder distributions can be calculated within a reasonable amount of time.

The top and bottom gates ( $V_{TG} = -V_{BG}$ ) are gated to effect individual carrier concentrations of  $10^{13} \text{ cm}^{-2}$  in each layer, which corresponds to a Fermi energy in the top (bottom) layer of 0.4 eV (−0.4 eV). The gate bias conditions and the interlayer separation have been chosen so as to satisfy the conditions for room temperature pseudospin ferromagnetism [38]. Here, I focus on the regime where the layer electron and hole populations place the system firmly in the dense electron-hole regime where the electron-hole pairs are expected to form a BCS-type state. In practice, this is a nontrivial density to achieve, but is necessary for condensation. The electric field created ( $8 \times 10^6 \text{ V/cm}$ ) between the top and

bottom monolayers is slightly below the dielectric breakdown voltage for SiO<sub>2</sub> and is theoretically feasible. The transport characteristics of such a system are in stark contrast to the dilute limit of electron-hole densities, which can be described as a weakly interacting Bose system of excitons [41]. In order to collect a sufficient statistical distribution on the effects of vacancy distribution on the inter-layer transport properties of double-layer graphene, several randomized vacancy configurations for each concentration are examined in this work.

The three-dimensional Hamiltonian, as described in Chapter 5, begins with the atomistic tight-binding description of an individual graphene monolayer,

$$H_{TL} = \sum_{\langle i,j \rangle} \tau |i\rangle\langle j| + V_i |i\rangle\langle i|, \quad (6.1)$$

where lattice points  $i$  and  $j$  are first nearest neighbors.  $\tau = -3.03$  eV is the nearest neighbor hopping energy for the  $p_z$  orbital of graphene, which allows for the unique low-energy linear dispersion at the  $K$  and  $K'$  points in the Brillouin zone shown in Fig. 4.2. Hopping among further nearest neighbors and other orbitals is neglected, because nearest neighbor  $p_z$  orbital hopping is the predominant interaction for graphene in the probed energy range of  $E_D \pm 1$  eV. The on-site potential energy  $V_i = \phi(\vec{r}_i)$  is calculated via a three-dimensional Poisson solver given in Eq. 5.1. The contact self-energy matrices use a phenomenological model to simulate a generic metal contact with a constant density of states [30; 42]. This model captures the basic self-energy needed to appropriately simulate a metal contact without taking into account multiple orbitals or complex interface problems such as lattice mismatch or Schottky barrier height.

The monolayer Hamiltonian is expanded to the double-layer Hamiltonian by coupling the top and bottom monolayers with the following Bogoliubov-de Gennes (BdG) Hamiltonian,

$$\mathcal{H}_{BdG} = \begin{bmatrix} H_{TL} & 0 \\ 0 & H_{BL} \end{bmatrix} + \sum_{\mu=x,y,z} \hat{\mu} \cdot \vec{\Delta} \otimes \sigma_{\mu}, \quad (6.2)$$

with the interlayer interactions including both single particle tunneling and the mean-field many-body contribution,  $\vec{\Delta}$ , coupling the two layers using a local density approximation. In Eq. 6.2,  $\mu$  represents a vector that isolates each of the Cartesian components of the pairing vector,  $\sigma_{\mu}$  represents the Pauli spin matrices in each of the three spatial directions, and  $\otimes$  represents the Kronecker product.

In order to correctly account for the dynamics of the double-layer graphene system, I first include the many-body interlayer interactions in the Hamiltonian. Within the Hartree-Fock mean-field approximation, the interlayer interactions may be defined through the expectation value of the full Hamiltonian,

$$\langle \uparrow_i | H_{BdG} | \downarrow_j \rangle = U m_{exc} \delta_{i,j}. \quad (6.3)$$

The graphene monolayers are assumed to be perfectly registered, so that electrons at site  $i$  in the top layer ( $|\uparrow_i\rangle$ ) only bind with holes at site  $j$  on the bottom layer ( $|\downarrow_j\rangle$ ) when  $i = j$ .  $U$  is the strength of the interlayer on-site Coulomb interaction, whose selected value is addressed later in this section.

The magnitude of the order parameter resulting from the analysis of BECs of indirectly bound excitons is  $m_{exc}$ . It is proportional to the off-diagonal terms in the single-particle density matrix, which is represented as [13; 39]

$$\rho = \begin{bmatrix} \rho_{\uparrow\uparrow} & \rho_{\uparrow\downarrow} \\ \rho_{\downarrow\uparrow} & \rho_{\downarrow\downarrow} \end{bmatrix}. \quad (6.4)$$

The on-diagonal density matrix ( $\rho_{\uparrow\uparrow}, \rho_{\downarrow\downarrow}$ ) corresponds to the associated electron and hole densities of the top and bottom monolayers, respectively. The order parameter  $m_{exc}$  can now be defined as a function of the interlayer component of the density matrix,

$$\begin{aligned} m_{exc}^x &= \rho_{\uparrow\downarrow} + \rho_{\downarrow\uparrow} = 2\text{Re}(\rho_{\uparrow\downarrow}), \\ m_{exc}^y &= -i\rho_{\uparrow\downarrow} + i\rho_{\downarrow\uparrow} = 2\text{Im}(\rho_{\uparrow\downarrow}). \end{aligned} \quad (6.5)$$

The density matrix is directly calculated within the NEGF formalism. It is consequently both an input and an output of the simulation, and the algorithm must iterate over the above mean-field equations, in conjunction with the Poisson equation for electrostatics, to obtain a self-consistent solution with compatible particle densities and potential profile. The Broyden method [43] is utilized to expedite numerical convergence.

Equation 6.2 can be expanded to show a simplified form for the BdG Hamiltonian in which interlayer interactions are expressed in terms of their directional



components [44],

$$\mathcal{H}_{BdG} = \begin{bmatrix} H_{TL} + \Delta_z & \Delta_x - i\Delta_y \\ \Delta_x + i\Delta_y & H_{BL} - \Delta_z \end{bmatrix}. \quad (6.6)$$

The directional components of the interlayer interactions  $\vec{\Delta}$  are expressed as

$$\begin{aligned} \Delta_x &= (\Delta_{sas} + Um_{exc}^x) \\ \Delta_y &= Um_{exc}^y \\ \Delta_z &= \frac{1}{2}(V_{\uparrow} | i \rangle \langle i | - V_{\downarrow} | i \rangle \langle i |). \end{aligned} \quad (6.7)$$

The on-diagonal term in the interlayer interactions,  $\Delta_z$ , is due to screening caused by the unbound carriers in each monolayer, and acts to separate the two Fermi surfaces. The value of the single particle tunneling energy,  $\Delta_{sas}$ , is proportional to the probability of a single electron tunneling through the thin dielectric and recombining with a hole. Single-particle tunneling is an adverse event; thus it is desirable to have a very thick barrier in between the two graphene layers to maximize the lifetime of the indirectly bound excitons. However, a strong interlayer Coulomb interaction is needed to drive the superfluid phase transition, which necessitates a thin barrier. In this work, I set  $\Delta_{sas} = 1 \mu\text{eV}$  sufficiently small so that the lifetime of the indirectly bound exciton is long enough to observe condensation but not so small as to require an intractably large number of iterations before self-consistency is reached.

Results of previous many-body calculations show the value of the order parameter is approximately one-tenth the Fermi energy [38]. The simulations show that this value of  $m_{exc}$  corresponds to an interlayer coupling strength of 2.0 eV. Although this is less than the unscreened mean-field interaction strength [13] ( $U = \frac{q^2}{\epsilon d} \approx 4.6 \text{ eV}$ ), it is more plausible because it factors in damping effects due to screening [45]. The interlayer Coulomb interaction is thus set to  $U = 2.0 \text{ eV}$  in all simulations to be compatible with the mean-field theory. The magnitude of the order parameter, using the expectation values of the density matrix in Eq. 6.5, is

$$|m_{exc}| = \sqrt{(m_{exc}^x)^2 + (m_{exc}^y)^2} \quad (6.8)$$

The phase of the order parameter is similarly dependent on the same expectation

values of the density matrix [44],

$$\phi_{exc} = \tan^{-1} \left[ \frac{m_{exc}^y}{m_{exc}^x} \right]. \quad (6.9)$$

As the interlayer transport properties are similar to the case of a Josephson junction, the phase is expected to be  $\phi_{exc} = \pi/2$  at zero bias to maximize interlayer current [46; 47]. The quasiparticle and condensate current densities, the artifacts of the Andreev reflection action, are proportional to the spatial phase gradient and magnitude of the order parameter [13].

## 6.2 The Ideal System

All simulations are run in the drag-counterflow geometry ( $V_{TL} = -V_{TR}$ ;  $V_{BL} = V_{BR} = 0$  V) [13] to induce an effective current through the bottom layer only when the condensate exists, as described in Section 3.1. All non-equilibrium configurations described below are in this geometry, with the left and right contacts on the top monolayer set to the magnitude of the counterflow bias parameter. The entire process results in a condensate current, due to the propagating exciton, and a quasiparticle current, caused by the injected and retro-reflected individual carriers. The quasiparticle current is only nonzero within the coherence length ( $L_c$ ), the maximum length an injected particle penetrates into the superfluid gap before triggering the exciton scattering event. The microscopic attributes of the superfluid and the dynamics of the Andreev reflection may not be readily apparent in experiments, but will have a macroscopic effect on the observable interlayer current.

These observable interlayer and intralayer transport properties are presented for an ideal system in Fig. 6.1. The currents are odd functions of the bias, reflecting the system's ambipolar nature. At low bias, interlayer current is linear and interlayer conductance is constant, because injected carriers see the superfluid gap and trigger the Andreev event discussed above. Low-energy injected carriers are unable to pass through the superfluid gap, and intralayer current is negligible within this range. States above the superfluid band gap do begin to form at  $|E| \geq 0.14$  eV, as seen in the superfluid band structure in Fig. 6.2a. Interlayer transmission quickly vanishes when higher-energy states become accessible in the spectrum; transport along the monolayer dominates in these ranges. This is evidenced by the

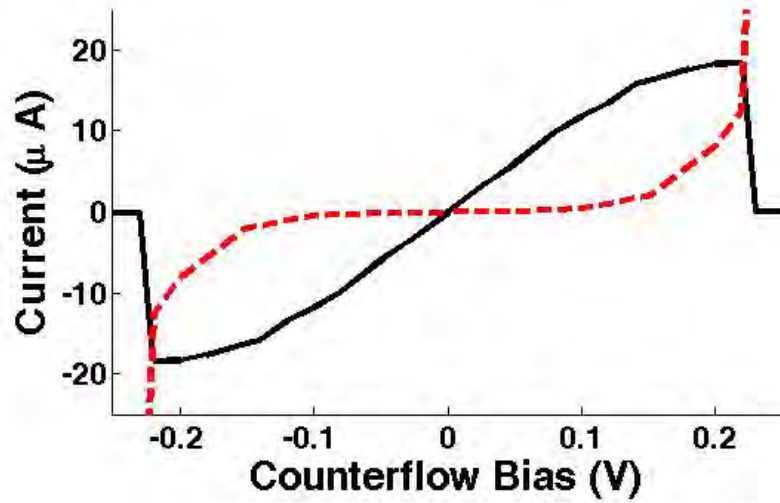


Figure 6.1: Interlayer and intralayer current plots for the ideal system as a function of counterflow bias (solid black line and red dashed line, respectively).

emergence of intralayer current and a drop in interlayer conductance beginning at a counterflow bias of 0.14 V.

Beyond the critical counterflow bias,  $0.22 \pm 0.01$  V in the ideal system, the superfluid can no longer adjust its phase to accommodate the current flow. When self-consistency is lost, only single-particle tunneling contributes to interlayer tunneling. The small magnitude of the resultant interlayer current, less than 1 pA for a bias of  $V_{TL} = -V_{TR} = 0.25$  V, is negligible compared to the many-body contribution to the interlayer current observed when the system obtains self-consistency. Additionally, past the critical current, transport characteristics become time-dependent [48], and the mean field equations no longer represent a valid description of the physics. Although a transient remnant of the superfluid may yet persist beyond the critical bias, the many-body portion of the Hamiltonian is approximately zero and the time dependent oscillation in the interlayer transport relationship cannot be captured in the steady-state simulations.

The phase transition is observed in Fig. 6.2b, which shows the dispersion for the ideal system after critical current has been passed. There is no appreciable change to the band structure within each phase. When no superfluid exists, each monolayer has a vanishing band gap and linear dispersion, as seen in Fig. 4.2. As expected, the Dirac points occur in the normal phase at the K' and K points in the Brillouin zone with a Fermi energy of  $\pm 0.4$  eV. The band gap vanishes at biases

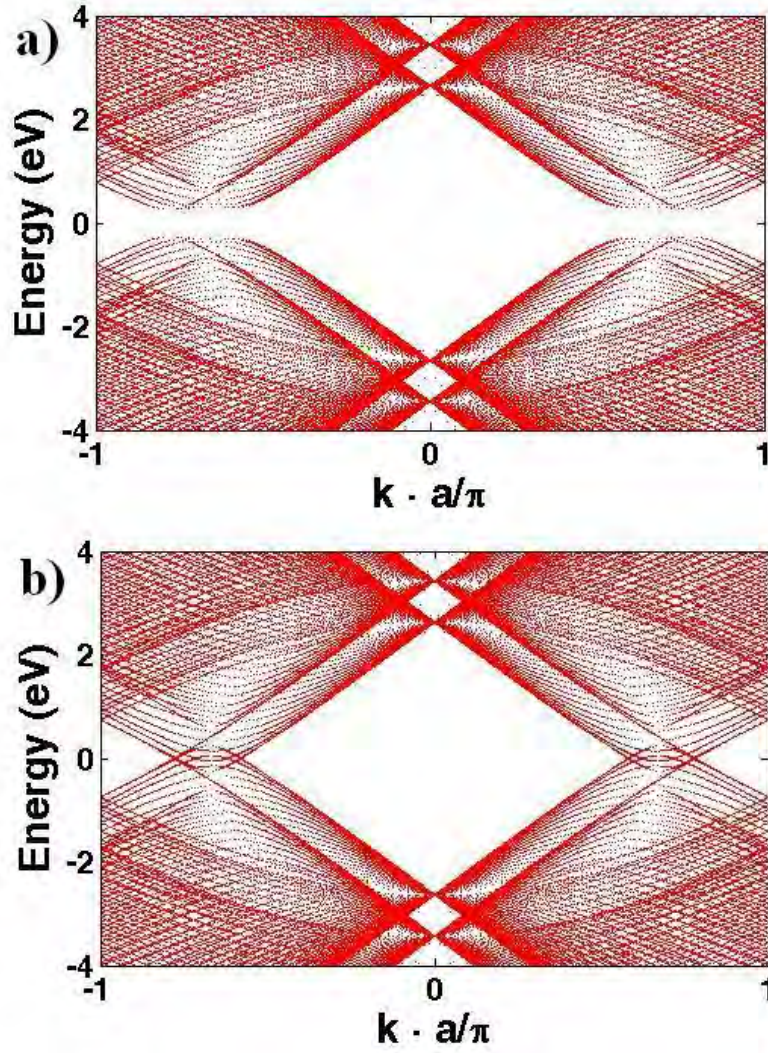


Figure 6.2: The dispersion relation for an ideal double-layer graphene system in the transport direction (a) at a counterflow bias of  $V_{TL} = -V_{TR} = 0.05$  V, which is below the critical current and (b) at a counterflow bias of  $V_{TL} = -V_{TR} = 0.23$  V, which is above the critical current.

larger than this critical transition value. The closing of the band gap after the phase transition allows for more low-energy states, causing a spike in intralayer current well beyond the range of interlayer transport in the superfluid phase.

The band structure in the transport direction of the system is derived [49] from a small portion of the converged Hamiltonian by assuming  $m_{exc}$  is periodic in the transport direction. This holds true only for the ideal system, where  $m_{exc}$  is smooth and consistent throughout the channel with a magnitude near 10% of the Fermi energy and a phase of  $\pi/2$ . Randomly placed impurities and vacancies, however, break translational symmetry so that the Hamiltonian is no longer periodic in the transport direction. The dispersion relations of disordered systems thus cannot be calculated.

The ideal system's critical current is calculated to be  $I_c = \pm 18.4 \mu\text{A}$ , occurring at a counterflow bias of  $\pm 0.22 \text{ V}$ . The analytic approximation for the critical current in a system where coherence length is smaller than system length [48] can be evaluated by ensuring the condensate satisfies the elliptic sine-Gordon equation,

$$\lambda^2 \vec{\nabla}^2 \phi - \sin(\phi) = 0. \quad (6.10)$$

When this equation is solved in the static (DC) case, the critical current of the system simplifies to a relatively simple expression,

$$I_c \sim \frac{eWm_{exc}}{\hbar L_c}. \quad (6.11)$$

Therefore, for a system of width  $W = 10 \text{ nm}$  with a coherence length of  $L_c \approx 5 \text{ nm}$  and order parameter magnitude of  $\rho_s \approx 0.04 \text{ eV}$ , the analytic critical current is roughly  $I_c^A \approx 19.5 \mu\text{A}$ . This is in good agreement with the simulated critical current for an ideal system. The reduction in the critical current is expected in the system as reflections off the superfluid gap lead to enhanced differences in local interlayer interaction terms which enter into the Hamiltonian self-consistently through the  $\Delta_z$  term and serve to energetically separate the layers [44].

Figure 6.3 plots the interlayer quasiparticle current densities along the transport direction averaged along the width of the system in an ideal system with a counterflow bias of  $0.05 \text{ V}$  and  $0.20 \text{ V}$ , just before the phase transition to a normal state. Quasiparticle current tunneling, which is part of the same process that launches the exciton through the channel, is highest near the contacts where carriers are injected, and evanescently decays into the channel, so that carriers which provoke

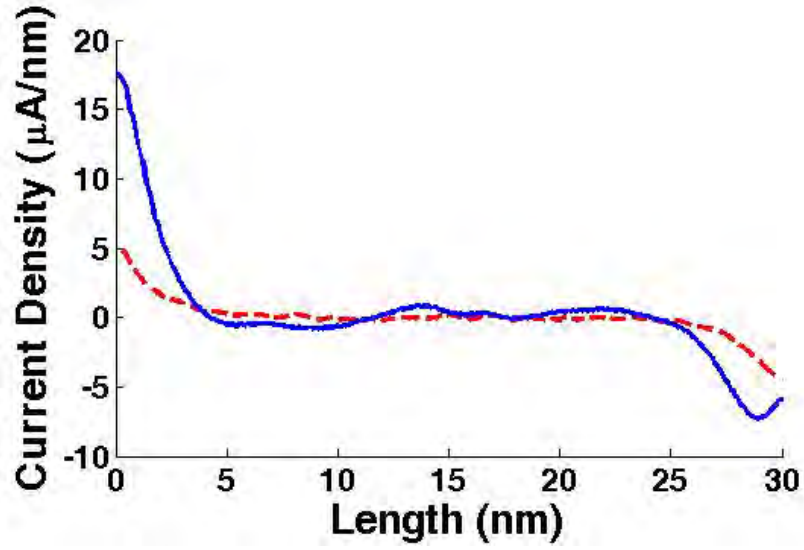


Figure 6.3: The interlayer quasiparticle current density along the transport direction in the ideal system averaged along the width of the system for counterflow biases of 0.05 V (red dashed line) and 0.20 V (blue solid line). The current density is only nonzero within the coherence length, which by inspection is approximately 5 nm. Quasiparticle current density is approximately odd about the center of the system at low bias, but symmetry is lost when a high contact bias limits carrier concentration on one side of the system.

interlayer transmission are only present a small distance into the channel. This distance, termed the coherence length ( $L_c$ ), is roughly 5 nm by inspection of the plot.

Note in Fig. 6.3 that interlayer quasiparticle current magnitude is nearly equivalent at low bias but becomes very asymmetric near the critical transition point. The Poisson equation in the counterflow bias configuration restricts the magnitude of the order parameter because the negatively biased top right contact locally decreases the density of electrons able to pair into the condensate. Conversely, applying a bias across the hole-doped bottom layer will limit superfluid density and quasiparticle current near the left (positively biased) contact. The decreased density results in a smaller interlayer current density on one side, as seen in the case with higher counterflow bias. All interlayer currents are the currents generated by the contacts on the right side of the system, because this is the side with limited exciton density is the transport bottleneck. When the disparity in condensate currents from each contact reaches a critical limit, steady-state supercurrents are no longer possible [13].

### 6.3 Disordered Systems

I now seek to understand how the behavior of the interlayer transport properties change as disorder is introduced into the system. The main result of the analysis is shown in Fig. 6.4, which plots the statistical variation in critical current as a function of vacancy concentration. Two distinct categories of disorder in the top layer are considered. The critical current obtained for the ideal case is plotted in the middle of the figure, at a vacancy concentration of 0%. To the left of the ideal case, the statistical variation in the critical current is plotted for random vacancy concentrations which are beyond the coherence length,  $L_c$ , from either contact on the top layer. In this case, an increase in the random vacancy concentrations causes a decrease in the critical current approximately following a square root dependence. Furthermore, the mean of the statistical distribution of critical currents associated with various top layer vacancy distributions varies only by approximately 5% even as the concentration of vacancies is increased.

The statistical change of the critical current associated with disorder within a distance of  $L_c$  from either top layer contact is plotted on the right hand side of Fig. 6.4. Here quite different behavior is observed compared to the situation

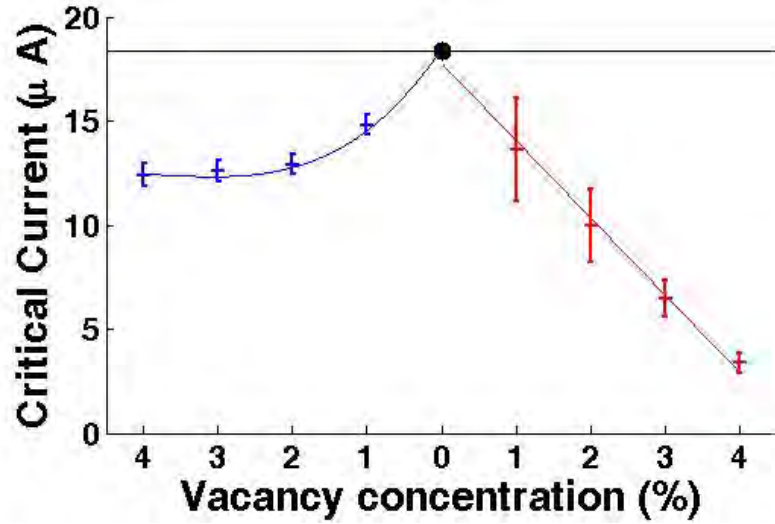


Figure 6.4: Statistical variation of critical interlayer current for several runs at the bias just before the condensate is broken. Vacancies which are more than a distance of one coherence length away from the top layer contacts are to the left of the ideal (0%) case, depicted by a black circle, while vacancies which are within one coherence length from the top layer contacts are to the right. The excitonic condensate is lost in both cases for top layer vacancy concentrations larger than 4%. The solid lines represent analytic calculations using Eq. 6.11 with modified values obtained from calculations as described in Section 6.3.



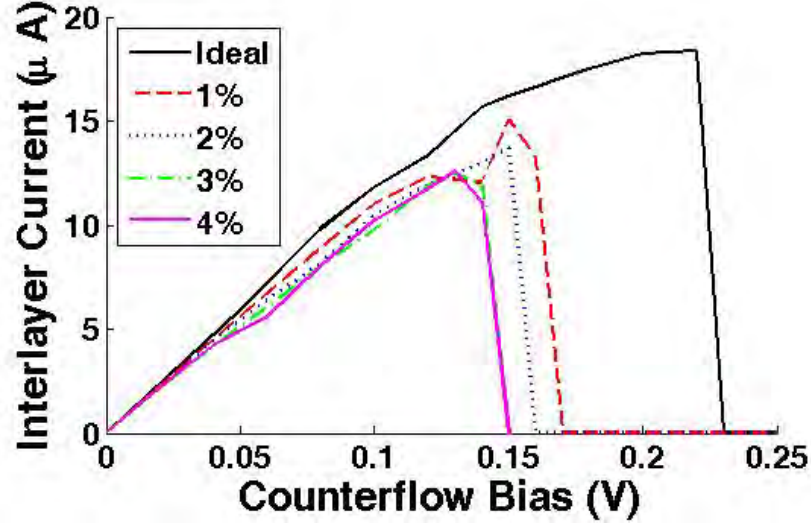


Figure 6.5: Set of I-V curves for systems with varying concentrations of randomly placed vacancies at least 5 nm away from the top layer contacts.

where the vacancies are further than  $L_c$  from the top layer contacts. Now the critical current has a very distinct linear decrease with respect to an increase in vacancy concentrations. There are very large variations in the location of the critical current, which is dependent on the locations of the top layer vacancies. In the subsequent sections, I will explore the physics of these two distinct regions and explain the observed dependence of the critical current seen in each situation.

### 6.3.1 Layer Disorder beyond $L_c$

Disorder is modeled by randomly placing vacancies within the top layer of the double-layer system. Vacancies are modeled by setting all hopping to a missing atom to zero in the model Hamiltonian. This effectively blocks any interaction with the vacancy by setting the tight-binding overlap integral of the spatial  $p_z$  orbital states to zero [50]. A fixed percentage of carbon atoms are randomly removed from the specified region of the top monolayer, leaving the bottom monolayer unperturbed, and the transport calculations from the ideal case are repeated.

The interlayer current is plotted as a function of voltage bias in Fig. 6.5 for various concentrations of vacancies in the top layer along with the ideal double-layer case for comparison. At low bias, there is little reduction in the interlayer conductivity regardless of vacancy concentration or vacancy location past the coherence

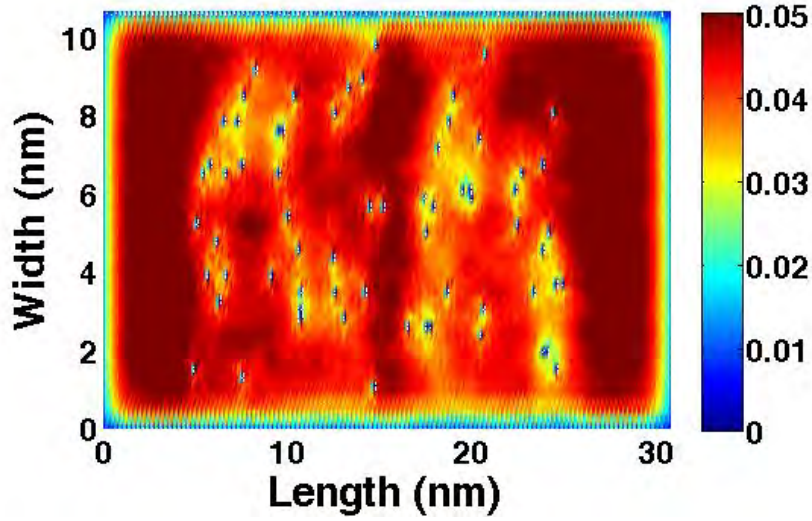


Figure 6.6: Magnitude of the order parameter for a system with 1% vacancies in the channel. The condensate is very close to that of the ideal case, with a drop in magnitude only occurring locally near disorder. As expected,  $|m_{exc}| \approx 0.1 E_F$  away from disorder.

length. The phase transition to two normal, incoherent Fermi liquids, however, occurs at a lower bias than in the ideal case. Channel disorder decreases critical current by 20% for 1% vacancy concentration to 30% for vacancy concentrations of 4%. Beyond top layer vacancy concentrations of 4%, no self-consistent solution is found and the interlayer transport is dominated by single-particle tunneling events. Resultant interlayer currents are orders of magnitude smaller because the majority of the current injected into the system now flows across the graphene layers.

In order to better understand these reductions in interlayer current as the top layer vacancy concentration is increased, I examine the magnitude of the order parameter,  $|m_{exc}|$ . In Fig. 6.6, the magnitude of the order parameter is plotted for a random vacancy concentration of 1%. In this situation, the order parameter magnitude does not remain constant over the entire system at  $10\% E_F$ , as was the case in the ideal system. The vacancies locally destroy the condensate [45] and reduce  $|m_{exc}|$  at surrounding points up to a distance of 0.5 nm, or three to four nearest neighbors from the vacancies. However, no long-range effect is seen when vacancies are isolated from one another by more than approximately 2 nm. At this particular vacancy concentration,  $m_{exc}$  is reduced by 40% over an appreciable area

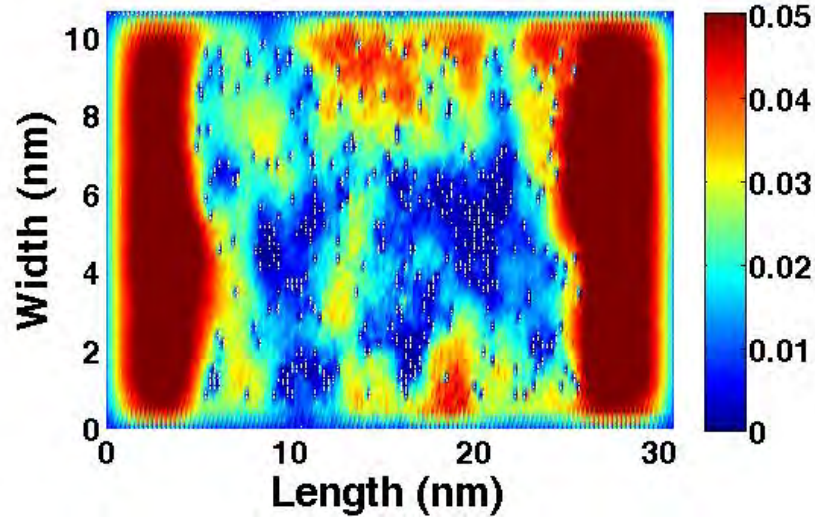


Figure 6.7: Magnitude of the order parameter for a system with 4% vacancies in the channel. Magnitude clearly drops nonlinearly with the increase in disorder, but quasiparticle current is still able to form near the contacts.

of the system as a result of these vacancies.

This situation is to be contrasted with Fig. 6.7, in which  $m_{exc}$  is plotted for a random top layer vacancy concentration of 4%. In this case, significant areas clearly emerge where concentrated disorder has long-range effects on superfluid density. These areas of high vacancy concentrations in Fig. 6.7 give rise to values for  $|m_{exc}|$  that are less than 20% the ideal value over significant areas of the system. Superfluid magnitude remains at its ideal level near the contacts, sufficiently quarantined from the vacancies.

Nevertheless, the root cause of the sublinear behavior in the critical current with respect to an increase in the top layer vacancy concentration remains unresolved, from Eq. 6.11. The localized density of states (LDOS) [51] is examined to explain the sublinear behavior. Vacancies induce a LDOS similar to the case of an impurity [52; 53] in graphene layers. Figures 6.8 and 6.9 plot the LDOS for the ideal case and for the case of 4% top layer vacancy concentration as an average along the disordered area of each monolayer. The average shows the magnitude of uncoupled states that form not only at vacancies, but at neighboring locations and in the ideal bottom layer as a result of electrostatics. A stark contrast is seen in the low-energy LDOS in the superfluid phase when vacancies are introduced. The LDOS closely resembles those of monolayer graphene at higher energies [54],

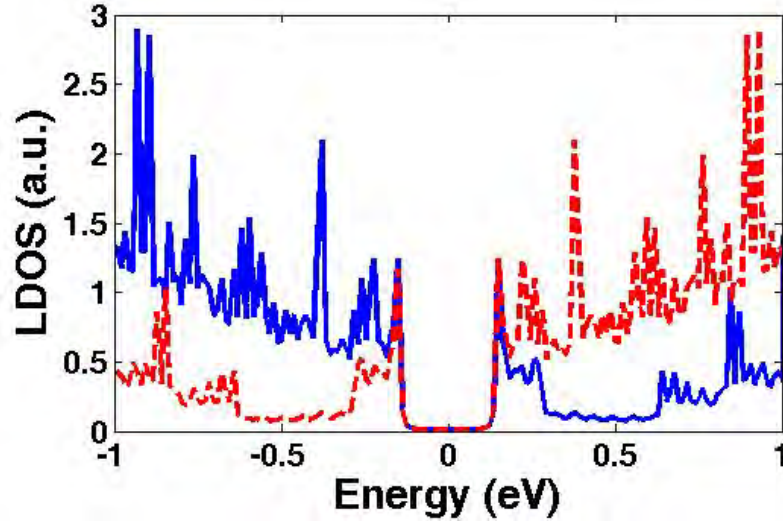


Figure 6.8: Local density of states at low energy for an ideal system. The solid (dashed) line represents the top (bottom) layer. No localized states exist below a magnitude of 0.14 eV for the superfluid.

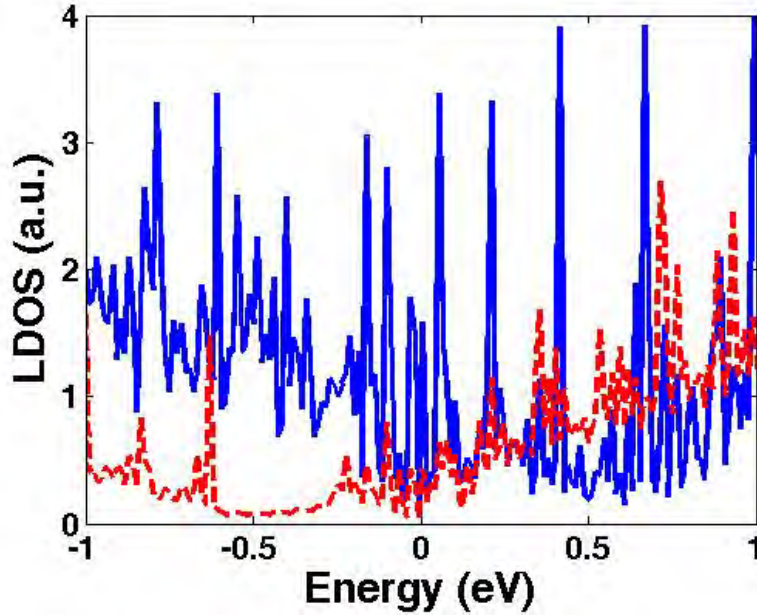


Figure 6.9: Local density of states at low energy for a system with 4% vacancies in the top layer. The solid (dashed) line represents the top (bottom) layer. Low-energy states due to the vacancies introduce a weak but apparent LDOS in the ideal bottom layer as well, due to the thinness of the spacer dielectric.

with peaks at  $E = E_F \pm \tau$ . The ideal top and bottom monolayers exhibit perfectly antisymmetric densities of states so that equivalent carrier concentrations arise in the oppositely gated top and bottom monolayers. No states exist in the superfluid gap in the ideal double-layer, as is expected for a condensate in which all of the quasiparticles participate.

Disorder changes the transport properties of the system by introducing mid-gap states in the top layer, as seen in Fig. 6.9. Localized states also arise, to a lesser degree, in the bottom layer due to charge pileup induced by Coulomb attraction through the thin spacer dielectric. The biased top and bottom gates, necessary to generate the sufficient carrier concentrations, cause the undesirable occupation of the mid-gap states up to the Fermi energy. As the electrons and holes make their way across the layers, they scatter off localized states, changing the interlayer phase relationship between the top and bottom layers. This effect manifests itself as a change in the  $\Delta_y$  term in Eq. 6.5. As a result, when the decreased interlayer phase relationship is input into the calculation of  $m_{exc}$  in Eq. 6.8,  $m_{exc}$  drops from its ideal value of 0.041 eV to  $0.029 \pm 0.002$  eV at 4% top layer vacancy concentration, a decrease of roughly 30%. The result is thus that the reduced interlayer phase component decreases  $m_{exc}$  in a rough square root correlation. The square root dependence is not exact and saturates at higher disorder concentrations because  $m_{exc}$  is not affected near the contact regions and is allowed to remain at its ideal value, as seen in Fig. 6.7. When the average value of the change in the coupling strength is added into the calculation of the critical current in Eq. 6.11 and plotted along with the numerical results on the left hand side of Fig. 6.4, good agreement is found between the two values. The average coupling strength does not change appreciably between disorder configurations, resulting in critical current approximations with small deviations relative to the contact disordered scenario.

### 6.3.2 Layer Disorder within $L_c$

While the double-layer graphene system is moderately robust to vacancies deep in the channel, this is not the case when the top layer vacancies occur within one  $L_c$  of the contacts on the top layer. The interlayer current is plotted as a function of the random top layer vacancy concentration in Fig. 6.10, where the vacancies occur within one  $L_c$  of the contacts on the top layer. Vacancies near the contacts cause a

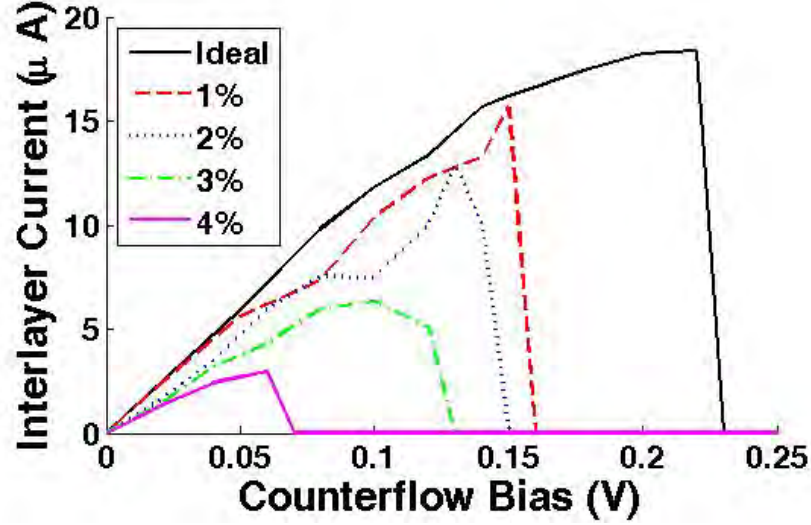


Figure 6.10: I-V curve for systems with varying concentrations of randomly placed vacancies within 5nm of the top layer contacts.

significant drop in both conductivity and the voltage bias at which self-consistency is lost. Quasiparticle current density is now dependent on the location of disorder within the coherence length, because magnitude evanescently decays from the contact interface. Interlayer current is thus sensitive to the specific location and amount of disorder within the coherence length.

Figure 6.11 shows the magnitude of the order parameter,  $m_{exc}$ , for a case of 1% vacancies randomly distributed near the contacts. Quasiparticle current density drops with the presence of contact disorder, because it is proportional to the magnitude of the order parameter. Clearly, groups of vacancies appear on the left and right side of the contact that begin to show a nonlinear, long-range effect on superfluid density. Top layer vacancies closest to the contact, where quasiparticle tunneling magnitude is largest, cause the biggest detriment to the magnitude of interlayer current. Despite the vacancies reducing the space in which quasiparticles may be injected without scattering, the condensate is able to form; sites within three nearest neighbors of a single defect are not appreciably affected. Little randomized bunching occurs in the 1% case, because the disorder is too sparse to create significantly different scenarios. Interlayer current remains rather robust, roughly 30% smaller than ideal. The random nature of the placement, however, causes a high variance in interlayer current in this scenario, which is discussed below.



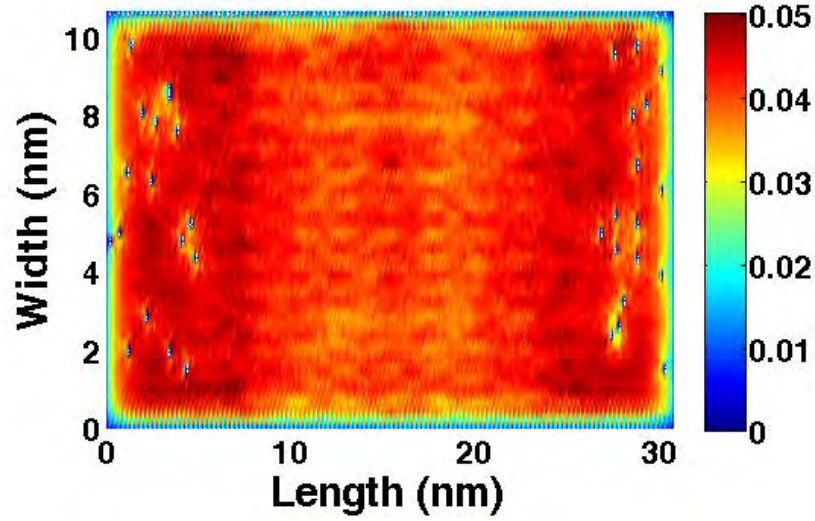


Figure 6.11: Magnitude of the order parameter, in eV, for a system subjected to 1% vacancies near the contacts. A single defect does not affect the condensate appreciably, but several defects nearby can drop magnitude significantly.

Larger deviations from the ideal interlayer critical current are found as the top layer vacancy concentration is increased. A large amount of clustering occurs, which leads to a significant reduction in the available space into which quasiparticles may be injected, as seen in Fig. 6.12, and generates a very different transport relationship relative to channel disorder. Carriers injected into the system see a significant reduction in the area in which quasiparticle tunneling can occur near the contact, significantly reducing conductivity. There is a linear dependence on the width of the system in Eq. 6.11, and this provides a very simple explanation for the physics of the linear decrease in the critical current observed in Fig. 6.4. This information allows us to conclude that graphene with vacancies within the coherence length effectively reduces the width over which quasiparticle tunneling occurs, and causes a linear decay in  $I_c$  with respect to contact disorder strength until the condensate vanishes.

Figure 6.13 shows how the average interlayer quasiparticle current density qualitatively shifts when top layer vacancies are included within the coherence length of the top layer contacts. Equivalent disorder concentrations generate disparate condensate currents on each side because vacancies are randomly configured to be more closely lumped near one contact than the other. Whereas superfluid excitons are able to permeate disorder as long as the condensate exists, an increasing pro-

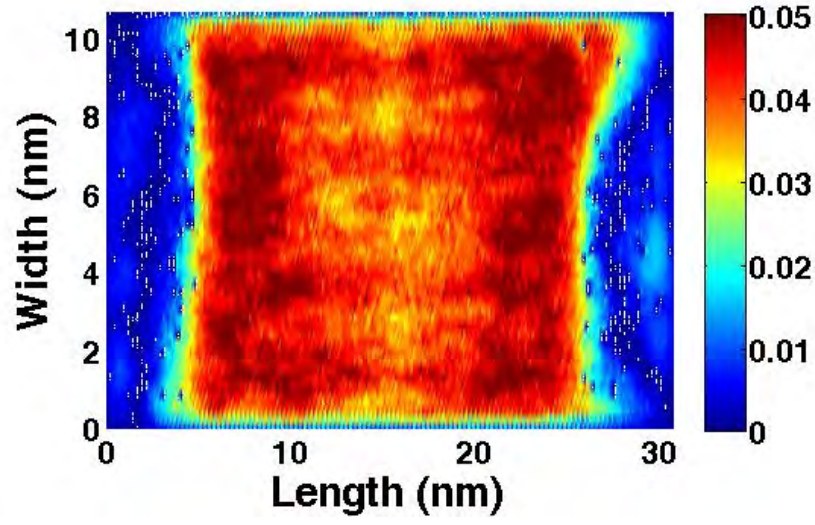


Figure 6.12: Magnitude of the order parameter, in eV, for a system subjected to 4% vacancies near the contacts. The contacts are too saturated with defects for a large amount of tunneling to occur, and interlayer conductivity suffers.

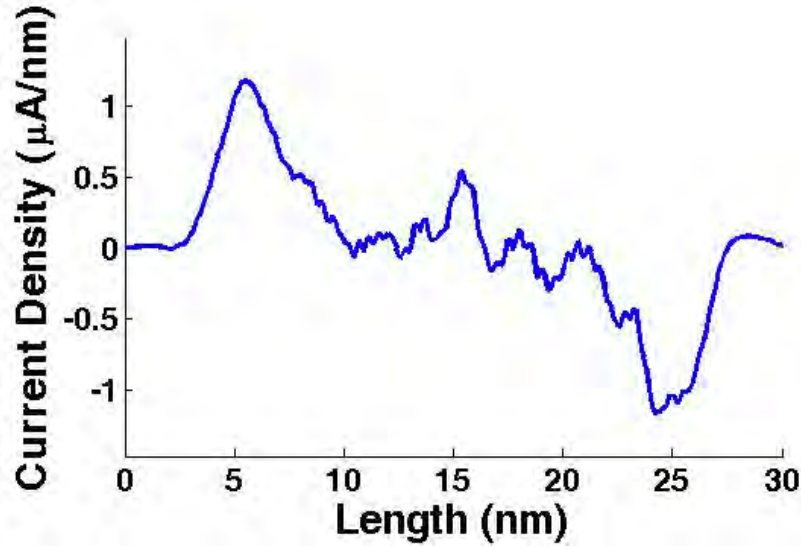


Figure 6.13: Quasiparticle current density for a system with 4% contact disorder with a counterflow bias of 0.04 V, just before the phase transition. No condensate exists near the contacts, so the largely degraded quasiparticle tunneling that does occur only happens beyond the disorder.



portion of bare electrons and holes cannot penetrate the contact disorder to reach the condensate. The critical bias at which the phase transition occurs decreases as disorder increases because of the discrepancy in condensate current from each contact. The on-site potential is greater at vacancies near the contacts due to  $V_{TR}$  and  $V_{TL}$ . The LDOS is thus more quickly occupied, and further accelerates the phase transition. As a result, critical current drops approximately by an average of 30%, 45%, 60%, and 80% for vacancy concentrations of 1%, 2%, 3%, and 4%, respectively. The accuracy of the conclusion can be seen on the right hand side of Fig. 6.4 where the data is superimposed with a model of the reduction of the critical current expected when each vacancy is assumed to remove 0.5 nm from the effective width of the system in the affected region for a given vacancy concentration. The theory and numerical calculations prove to be in good agreement; the model falls within the error bars of the simulations, where deviation is the result of non-linear randomized bunching of disorder.

It is clear in Fig. 6.4 that a large variance in critical current exists when vacancies lie within the coherence length of the contacts in the top layer. This is due to the fact that the quasiparticle current flow, in this system, is concentrated close to the contacts in the middle of the channel, and evanescently decays into the system. This is best seen in Fig. 6.11 where the magnitude of the order parameter is significantly reduced from the bulk value near the edge of the system both near and away from the contacts. Moreover, vacancies that are closely lumped together exacerbate the scattering to an even greater degree because vacancies in close proximity to one another have a significant non-local effect on the perturbed  $m_{exc}$ , as seen in Fig. 6.12. Also in Fig. 6.12, the variance in critical current decays at 4% vacancies because quasiparticle tunneling is almost completely prevented at such a high concentration of vacancies. As in the channel-disordered case, no self-consistent solution was found for vacancy concentrations greater than 4%.

# CHAPTER 7

## CONCLUSION

Superfluid transport is an observed phenomenon in BECs in which bosons flow through a channel without dissipation. Many-body transport in such a system can lead to efficiencies and speeds beyond the fundamental limit of conventional CMOS technology. The performance enhancement could be realized in the electronic systems that have become so ubiquitous in telecommunications, computing, processing, and information technology. This thesis studies self-consistent calculations to understand how vacancies in the graphene monolayer channel can hinder such performance of a predicted room-temperature exciton condensate. Vacancies within a coherence length of the contacts significantly obstruct performance by effectively reducing the width over which interlayer transport occurs. For a selected value of 4% vacancies in this region, tunneling current at a selected bias can drop by more than 80% compared to the ideal scenario. The reduced width of the system caused by the presence of the top layer vacancies produces a linear dependence on the critical current as the vacancy concentration is increased. Vacancies outside of the coherence length have little effect on the interlayer conductivity, showing a critical current with an approximate square root dependence on vacancy concentration in the top layer. Critical current degrades up to 30% due to a phase transition at smaller bias. The reduction is due to scattering of layer quasiparticles from localized mid-gap states, which modifies the average interlayer phase relationship between the two layers. Concentrations of vacancies larger than 4% in one of the layers prevent the condensate from forming in a steady state.

The thesis thus provides a concise model to show how channel disorder affects superfluid transport. As the ideal system is difficult to realize, it provides experimentalists a numerical framework for characterizing fabricated systems dominated by short-range scattering impurities. Future work includes adding the effect of phonon scattering to the lattice to see how superfluid density and critical tunneling current decay as temperature increases. Aside from lattice disorder, phonon

coupling to the substrate is a dominant scattering mechanism that must be studied in order to have a complete picture of room-temperature performance degradation from an ideal system.

## REFERENCES

- [1] G. E. Moore, “Cramming more components onto integrated circuits,” *Electronics*, vol. 38, no. 8, pp. 114–117, 1965.
- [2] J. Bardeen, L. N. Cooper, and J. R. Schrieffer, “Microscopic theory of superconductivity,” *Phys. Rev.*, vol. 106, pp. 162–164, Apr 1957. [Online]. Available: <http://link.aps.org/doi/10.1103/PhysRev.106.162>
- [3] C. W. Chu, L. Gao, F. Chen, Z. J. Huang, R. L. Meng, and Y. Y. Xue, “Superconductivity above 150 K in  $\text{HgBa}_2\text{Ca}_2\text{Cu}_3\text{O}_{8+\delta}$  at high pressures,” *Nature*, vol. 365, pp. 323–325, 1993.
- [4] M. H. Anderson, J. R. Ensher, M. R. Matthews, C. E. Wieman, and E. A. Cornell, “Observation of Bose-Einstein condensation in a dilute atomic vapor,” *Science*, vol. 269, no. 5221, pp. 198–201, 1995. [Online]. Available: <http://www.sciencemag.org/content/269/5221/198.abstract>
- [5] J. Kasprzak, M. Richard, S. Kundermann, A. Baas, P. Jeambrun, J. M. J. Keeling, F. M. Marchetti, M. H. Szymanska, R. Andre, J. L. Staehli, V. Savona, P. B. Littlewood, B. Deveaud, and L. S. Dang, “Bose-Einstein condensation of exciton polaritons,” *Nature*, vol. 443, pp. 409–414, 2006.
- [6] H. Deng, H. Haug, and Y. Yamamoto, “Exciton-polariton Bose-Einstein condensation,” *Rev. Mod. Phys.*, vol. 82, pp. 1489–1537, May 2010. [Online]. Available: <http://link.aps.org/doi/10.1103/RevModPhys.82.1489>
- [7] S. Christopoulos, G. B. H. von Högersthal, A. J. D. Grundy, P. G. Lagoudakis, A. V. Kavokin, J. J. Baumberg, G. Christmann, R. Butté, E. Feltin, J.-F. Carlin, and N. Grandjean, “Room-temperature polariton lasing in semiconductor microcavities,” *Phys. Rev. Lett.*, vol. 98, p. 126405, Mar 2007. [Online]. Available: <http://link.aps.org/doi/10.1103/PhysRevLett.98.126405>
- [8] J. J. Baumberg, A. V. Kavokin, S. Christopoulos, A. J. D. Grundy, R. Butté, G. Christmann, D. D. Solnyshkov, G. Malpuech, G. Baldassarri Höger von Högersthal, E. Feltin, J.-F. Carlin, and N. Grandjean, “Spontaneous polarization buildup in a room-temperature polariton laser,” *Phys. Rev. Lett.*, vol. 101, p. 136409, Sep 2008. [Online]. Available: <http://link.aps.org/doi/10.1103/PhysRevLett.101.136409>

- [9] A. Bijl, J. de Boer, and A. Michels, “Properties of liquid helium II,” *Physica*, vol. 8, no. 7, pp. 655 – 675, 1941. [Online]. Available: <http://www.sciencedirect.com/science/article/pii/S0031891441904226>
- [10] A. Amo, D. Sanvitto, F. P. Laussy, D. Ballarini, E. d. Valle, M. D. Martin, A. Lemaitre, J. Bloch, D. N. Krizhanovskii, M. S. Skolnick, C. Tejedor, and L. Vina, “Collective fluid dynamics of a polariton condensate in a semiconductor microcavity,” *Nature*, vol. 457, pp. 291–295, 2009.
- [11] M. J. Gilbert, “Performance characteristics of scaled bilayer graphene pseudospin devices,” *IEEE Trans. Elect. Dev.*, vol. 57, p. 3059, 2010.
- [12] A. F. Andreev, “Thermal conductivity of the intermediate state of superconductors,” *Sov. Phys. JETP*, vol. 19, no. 5, pp. 1228–1231, 1964.
- [13] J. J. Su and A. H. MacDonald, “How to make a bilayer exciton condensate flow,” *Nature Physics*, vol. 4, pp. 799–802, 2008.
- [14] K. v. Klitzing, G. Dorda, and M. Pepper, “New method for high-accuracy determination of the fine-structure constant based on quantized Hall resistance,” *Phys. Rev. Lett.*, vol. 45, pp. 494–497, Aug 1980. [Online]. Available: <http://link.aps.org/doi/10.1103/PhysRevLett.45.494>
- [15] E. Tutuc, M. Shayegan, and D. A. Huse, “Counterflow measurements in strongly correlated GaAs hole bilayers: Evidence for electron-hole pairing,” *Phys. Rev. Lett.*, vol. 93, p. 036802, 2004.
- [16] R. D. Wiersma, J. G. S. Lok, S. Kraus, W. Dietsche, K. von Klitzing, D. Schuh, M. Bichler, H. P. Tranitz, and W. Wegscheider, “Activated transport in the separate layers that form the  $\nu = 1$  exciton condensate,” *Phys. Rev. Lett.*, vol. 93, p. 266805, 2004.
- [17] L. Tiemann, W. Dietsche, M. Hauser, and K. von Klitzing, “Critical tunneling currents in the regime of bilayer excitons,” *New J. Phys*, vol. 10, p. 045018, 2008.
- [18] L. Tiemann, J. G. S. Lok, W. Dietsche, K. von Klitzing, K. Muraki, D. Schuh, and W. Wegscheider, “Investigating the transport properties of the excitonic state in quasi-Corbino electron bilayers,” *Physica E - Low Dimensional Systems and Nanostructures*, vol. 40, pp. 1034–1037, 2008.
- [19] H. A. Fertig, “Energy spectrum of a layered system in a strong magnetic field,” *Phys. Rev. B*, vol. 40, pp. 1087–1095, 1989.
- [20] B. I. Halperin, P. A. Lee, and N. Read, “Theory of the half-filled Landau level,” *Phys. Rev. B*, vol. 47, pp. 7312–7343, 1993.

- [21] D. V. Fil and S. I. Shevchenko, “Interlayer tunneling and the problem of superfluidity in bilayer quantum Hall systems,” *Low Temp. Phys.*, vol. 33, pp. 780–782, 2007.
- [22] A. H. MacDonald, “Superfluid properties of double-layer quantum Hall ferromagnets,” *Physica B*, vol. 289, p. 129, 2001.
- [23] T. Jungwirth and A. H. MacDonald, “Resistance spikes and domain wall loops in Ising quantum Hall ferromagnets,” *Phys. Rev. Lett.*, vol. 87, p. 216801, 2001.
- [24] L. Tiemann, J. G. S. Lok, W. Dietsche, K. von Klitzing, K. Muraki, D. Schuh, and W. Wegscheider, “Exciton condensate at a total filling factor of one in Corbino two-dimensional electron bilayers,” *Phys. Rev. B*, vol. 77, p. 033306, 2008.
- [25] D. Snoke, “Spontaneous Bose coherence of excitons and polaritons,” *Science*, vol. 298, p. 1368, 2002.
- [26] I. B. Spielman, J. P. Eisenstein, L. N. Pfeiffer, and K. W. West, “Resonantly enhanced tunneling in a double-layer quantum Hall ferromagnet,” *Phys. Rev. Lett.*, vol. 84, p. 5808, 2000.
- [27] Y. Yoon, L. Tiemann, S. Schmult, W. Dietsche, K. von Klitzing, and W. Wegscheider, “Interlayer tunneling in counterflow experiments on the excitonic condensate in quantum Hall bilayers,” *Phys. Rev. Lett.*, vol. 104, p. 116802, 2010.
- [28] L. Tiemann, Y. Yoon, W. Dietsche, K. von Klitzing, and W. Wegscheider, “Dominant parameters for the critical tunneling current in bilayer exciton condensates,” *Phys. Rev. B*, vol. 80, p. 165120, 2009.
- [29] P. R. Wallace, “The band theory of graphite,” *Phys. Rev.*, vol. 71, no. 9, pp. 622–634, May 1947.
- [30] J. Guo, “Carbon nanotube electronics: Modeling, physics, and applications,” Ph.D. dissertation, Purdue University, West Lafayette, IN, 2005.
- [31] K. S. Novoselov, A. K. Geim, S. V. Morozov, D. Jiang, Y. Zhang, S. V. Dubonos, I. V. Grigorieva, and A. A. Firsov, “Electric field effect in atomically thin carbon films,” *Science*, vol. 306, no. 5696, pp. 666–669, 2004. [Online]. Available: <http://www.sciencemag.org/content/306/5696/666.abstract>
- [32] K. S. Novoselov, Z. Jiang, Y. Zhang, S. V. Morozov, H. L. Stormer, U. Zeitler, J. C. Maan, G. S. Boebinger, P. Kim, and A. K. Geim, “Room-temperature quantum Hall effect in graphene,” *Science*, vol. 315, no. 5817, p. 1379, 2007. [Online]. Available: <http://www.sciencemag.org/content/315/5817/1379.abstract>

- [33] A. H. Castro Neto, F. Guinea, N. M. R. Peres, K. S. Novoselov, and A. K. Geim, “The electronic properties of graphene,” *Rev. Mod. Phys.*, vol. 81, pp. 109–162, Jan 2009. [Online]. Available: <http://link.aps.org/doi/10.1103/RevModPhys.81.109>
- [34] J.-H. Chen, C. Jang, S. Xiao, M. Ishigami, and M. S. Fuhrer, “Intrinsic and extrinsic performance limits of graphene devices on SiO<sub>2</sub>,” *Nat. Nano*, vol. 3, pp. 206–209, 2008.
- [35] X. Li, W. Cai, J. An, S. Kim, J. Nah, D. Yang, R. Piner, A. Velamakanni, I. Jung, E. Tutuc, S. K. Banerjee, L. Colombo, and R. S. Ruoff, “Large-area synthesis of high-quality and uniform graphene films on copper foils,” *Science*, vol. 324, no. 5932, pp. 1312–1314, 2009. [Online]. Available: <http://www.sciencemag.org/content/324/5932/1312.abstract>
- [36] C. H. Zhang and Y. N. Joglekar, “Excitonic condensation of massless fermions in graphene bilayers,” *Phys. Rev. B*, vol. 77, p. 233405, 2008.
- [37] M. J. Gilbert and J. Shumway, “Probing quantum coherent states in bilayer graphene,” *J. Comput. Electron.*, vol. 8, pp. 51–59, 2009.
- [38] H. K. Min, R. Bistritzer, J. J. Su, and A. H. MacDonald, “Room-temperature superfluidity in graphene bilayers,” *Phys. Rev. B*, vol. 78, p. 121401, 2008.
- [39] S. Datta, *Quantum Transport: Atom to Transistor*. New York, NY: Cambridge University Press, 2005.
- [40] S. Datta, “Nanoscale device modeling: The Green’s function method,” *Superlattices and Microstructures*, vol. 28, no. 4, pp. 253 – 278, 2000. [Online]. Available: <http://www.sciencedirect.com/science/article/B6WXB-45JB2J1-3/2/d01b671a3bed65ff54b3b72447461fc8>
- [41] O. L. Berman, R. Y. Kezerashvili, and Y. E. Lozovik, “Bose-Einstein condensation of quasiparticles in graphene,” *Nanotechnology*, vol. 21, p. 134019, 2010.
- [42] G. Liang, N. Neophytou, M. S. Lundstrom, and D. E. Nikonov, “Contact effects in graphene nanoribbon transistors,” *Nano Letters*, vol. 8, no. 7, pp. 1819–1824, 2008. [Online]. Available: <http://pubs.acs.org/doi/abs/10.1021/nl080255r>
- [43] D. D. Johnson, “Modified Broyden method for accelerating convergence in self-consistent calculations,” *Phys. Rev. B*, vol. 38, pp. 12 807–12 813, 1988.
- [44] M. J. Gilbert, “Finite-temperature pseudospin torque effect in graphene bilayers,” *Phys. Rev. B*, vol. 82, no. 16, p. 165408, Oct 2010.

- [45] M. Y. Kharitonov and K. B. Efetov, “Electron screening and excitonic condensation in double-layer graphene systems,” *Phys. Rev. B*, vol. 78, p. 241401R, 2008.
- [46] E. Rossi, O. G. Heinonen, and A. H. MacDonald, “Dynamics of magnetization coupled to a thermal bath of elastic modes,” *Phys. Rev. B*, vol. 72, p. 174412, 2005.
- [47] K. Park and S. DasSarma, “Coherent tunneling in exciton condensates of bilayer quantum Hall systems,” *Phys. Rev. B*, vol. 74, p. 035338, 2006.
- [48] J. J. Su and A. H. MacDonald, “Critical tunneling currents in quantum Hall superfluids: Pseudospin-transfer torque theory,” *Phys. Rev. B*, vol. 81, p. 184523, 2010.
- [49] M. Luisier, A. Schenk, W. Fichtner, and G. Klimeck, “Atomistic simulation of nanowires in the  $sp^3d^5s^*$  tight-binding formalism: From boundary conditions to strain calculations,” *Phys. Rev. B*, vol. 74, no. 20, p. 205323, Nov 2006.
- [50] M. P. Anantram and T. R. Govindan, “Conductance of carbon nanotubes with disorder: A numerical study,” *Phys. Rev. B*, vol. 58, no. 8, pp. 4882–4887, Aug 1998.
- [51] N. Neophytou, S. Ahmed, and G. Klimeck, “Non-equilibrium Green’s function (NEGF) simulation of metallic carbon nanotubes including vacancy defects,” *J. Comput. Electron.*, vol. 6, pp. 317–320, 2007. [Online]. Available: <http://dx.doi.org/10.1007/s10825-006-0116-4>
- [52] V. M. Pereira, F. Guinea, J. M. B. Lopes dos Santos, N. M. R. Peres, and A. H. Castro Neto, “Disorder induced localized states in graphene,” *Phys. Rev. Lett.*, vol. 96, no. 3, p. 036801, Jan 2006.
- [53] A. Bácsi and A. Virosztek, “Local density of states and Friedel oscillations in graphene,” *Phys. Rev. B*, vol. 82, no. 19, p. 193405, Nov 2010.
- [54] S. Yuan, H. De Raedt, and M. I. Katsnelson, “Modeling electronic structure and transport properties of graphene with resonant scattering centers,” *Phys. Rev. B*, vol. 82, no. 11, p. 115448, Sep 2010.